AFRL-RH-WP-TR-2022-0057

MODULAR PLATFORM FOR DYNAMIC BIOCHEMICAL SENSING OF ACUTE SKIN WOUNDS

Francois Berthiaume, Mehdi Javanmard, Aaron Mazzeo

Rutgers, The State University of New Jersey

Kaushik Sengupta

Princeton University

MARCH 2022

Final Report

AIR FORCE RESEARCH LABORATORY
711TH HUMAN PERFORMANCE WING,
AIRMAN SYSTEMS DIRECTORATE,
WRIGHT-PATTERSON AIR FORCE BASE, OH 45433
AIR FORCE MATERIEL COMMAND
UNITED STATES AIR FORCE

NOTICE AND SIGNATURE PAGE

AFRL-RH-WP-TR-2022-0057 HAS BEEN REVIEWED AND IS APPROVED FOR PUBLICATION IN ACCORDANCE WITH ASSIGNED DISTRIBUTION STATEMENT.

//signature//	//signature//
JAMES VITAL, DR-III Chief, Airman Performance Section Performance Optimization Branch Airman Biosciences Division	R. ANDY MCKINLEY, DR-III, PhD Core Research Area Lead Cognitive and Physical Performance Performance Optimization Branch Airman Biosciences Division

REPORT DOCUMENTATION PAGE

Form Approved
OMB No. 0704-0188

1. REPORT DATE *(DD-MM-YY)*	2. REPORT TYPE	3. DATES COVERED *(From - To)*
31-03-22	Final	July 2020 – January 2022

4. TITLE AND SUBTITLE

Modular Platform for Dynamic Biochemical Sensing of Acute Skin Wounds

5a. CONTRACT NUMBER
FA8650-20-2-7032

5b. GRANT NUMBER

5c. PROGRAM ELEMENT NUMBER
00000F

6. AUTHOR(S)
*Francois Berthiaume, Mehdi Javanmard, Aaron Mazzeo
**Kaushik Sengupta

5d. PROJECT NUMBER

5e. TASK NUMBER

5f. WORK UNIT NUMBER
H129

7. PERFORMING ORGANIZATION NAME(S) AND ADDRESS(ES)
*Departments of Biomedical, Electrical & Computer, and Mechanical Engineering; Rutgers, The State University of New Jersey, Piscataway, NJ
**Department of Electrical Engineering; Princeton University, Princeton, NJ

8. PERFORMING ORGANIZATION REPORT NUMBER

9. SPONSORING/MONITORING AGENCY NAME(S) AND ADDRESS(ES)
Air Force Materiel Command
Air Force Research Laboratory
711th Human Performance Wing
Airman Systems Directorate
Airman Biosciences Division
Performance Optimization Branch
Wright-Patterson AFB, OH 45433

10. SPONSORING/MONITORING AGENCY ACRONYM(S)
711 HPW/RHBC

11. SPONSORING/MONITORING AGENCY REPORT NUMBER(S)
AFRL-RH-WP-TR-2022-0057

12. DISTRIBUTION/AVAILABILITY STATEMENT
Distribution Statement A: Approved for public release.

13. SUPPLEMENTARY NOTES
Report contains color. AFRL-2022-4072. Cleared 8 September 2022

14. ABSTRACT The purpose of this project was to develop reliable sensors that can report the concentration of key bioactive factors in wound fluid, and which can then be used for diagnosing and treating wounds, either by the physician, or as part of an eventual "smart bandage" that would use the sensor information to deliver treatments in an automated way. We developed sensor patches that are coated with antibodies for a specific antigen. Specific binding of the antigen to the sensor changes its impedance characteristics proportionally to the antigen concentration. We prepared sensors for inteleukin-6, tumor necrosis factor-, and albumin, and demonstrated their use on skin wounds in a standard mouse wound model. Different markers peaked at different times, thus providing biochemical information on the evolution of the wound healing. Sensor data were validated using standard biochemical assays. Sensors were also connected to a custom designed complementary metal-oxide-semiconductor (CMOS) chip, which enabled incorporation of the impedance analyzer in a bandage form factor, and will eventually allow collection of signals from multiple sensor patches. Time-resolved, on-demand sensor activation was achieved using graphene oxide membrane covers that were opened/ruptured by applying tunable vibration. While still more effort is necessary to understand the design, modeling, fabrication, and reliability of these membrane covers, these new results suggest potential for controllable rupture of membranes based on their diameter and thickness, along with their placement, bonding, and geometrical relationship to the substrate/device on which they reside. Using different membrane cover diameters that resonated at different frequencies provided a means to open covers in a specified sequence, thus allowing liquid samples to reach the desired sensor patches

15. SUBJECT TERMS enzyme-linked immunosorbent assays (ELISA), complementary metal-oxide-semiconductor (CMOS)

16. SECURITY CLASSIFICATION OF:			17. LIMITATION OF ABSTRACT:	18. NUMBER OF PAGES	19a. NAME OF RESPONSIBLE PERSON (Monitor)
a. REPORT	b. ABSTRACT	c. THIS PAGE			James Vital
Unclassified	Unclassified	Unclassified	SAR	52	19b. TELEPHONE NUMBER *(Include Area Code)* N/A

CONTENTS

List of Figures

SUMMARY

Skin wound healing proceeds via a series of overlapping phases, namely inflammation, proliferation, and remodeling. Different bioactive factors have been identified in these different phases; however, measuring them in the wound has been challenging and wound assessment by the practicing physician relies largely on gross wound appearance. The purpose of this project was to develop reliable sensors that can report the concentration of key bioactive factors in wound fluid, and which can then be used for diagnosing and treating wounds, either by the physician, or as part of an eventual "smart bandage" that would use the sensor information to deliver treatments in an automated way. We developed nanowell sensor patches, each consisting of an array of 5 x 5 nanowells coated with antibodies for a specific antigen. Specific binding of the antigen to the nanowell changes the impedance characteristics of the nanowells, and this change is proportional to concentration of antigen. We prepared sensors for interleukin-6, tumor necrosis factor-α, and albumin, and demonstrated their use on skin wounds in a standard excisional dorsal wound (1.5 centimeter (cm) x 1.5 cm) in wild-type mice. In this wound model, wound closure was complete after 14 days. The first two markers peaked at 3 days post-injury, reflecting the inflammatory phase of healing, and the last one peaked at days 7-10, which corresponds to the proliferative phase of healing. Measurements were carried out ex vivo, in wound fluid samples collected from the animals and assayed on the bench, as well as in situ with the sensors applied directly to the wounds. Sensor data were validated using independent commercial enzyme-linked immunosorbent assays (ELISA). It was not possible to measure wound fluid markers at 14 days post-injury or beyond since once the wound had closed, no wound fluid was expressed from the wound. The nanowell sensors were connected to a custom designed complementary metal-oxide-semiconductor (CMOS) chip, which enabled incorporation of the impedance analyzer in a bandage form factor, and also collection of signals from multiple sensor patches. Furthermore, in order to enable time-resolved measurements, nanowell patches were placed inside polydimethylsiloxane (PDMS) wells that were covered with graphene oxide membranes. A vibration generator placed near the membrane was used to open the membrane when the vibration frequency (f) matched the natural vibration frequency of the membrane, thus allowing fluid to drop onto the sensor patch. On-demand opening of different sensor patches could be achieved using different membrane diameters with different natural vibration frequencies. This approach allows opening different sensors at different times, either for time-resolved measurements, as well as when different markers are to be measured at different times. Further development of these technologies would seek integration into a more automated system that captures wound fluid levels of bioactive compounds over time in humans. The information would be used, together with other patient parameters (such as age, nutrition status, pre-existing morbidities or diseases), to determine which parameter(s), or combinations thereof, wound best correlate with wound healing outcome.

1 INTRODUCTION

1.1 Background and Hypothesis

Injured soldiers suffering from blast and burn injuries, who require treatment in a hospital environment typically take weeks to recover, thus significantly delaying their potential return to active duty and daily activities. Current acute wound care involves debridement, cleaning, antibiotic application, and covering with a sterile bandage that keeps the wound moist while absorbing excess exudate. Doctors use a combination of experience and trial-and-error to individualize treatments based on a visual qualitative assessment of the wound as well as the patient. This process is inefficient because it takes days before wound treatment is re-evaluated each time by the doctor. Furthermore, while the biology of wound healing and its associated signaling pathways have been characterized extensively, little of this information is actually used in making wound treatment decisions.

We hypothesize that wound healing can be significantly accelerated if wound pathophysiology is accurately diagnosed through the use of multiple quantitative measures of the wound environment. More specifically, sensors that report on local levels of key biological signaling molecules may be used to better stage and diagnose the wound healing state. This information will guide better therapeutic decisions, and in turn speed up wound healing. The sensor signals may also be used to drive decision algorithms and actuators in smart bandages, thus decreasing the frequency of direct interventions by doctors and nurses.

1.2 Purpose

Proof-of-concept for feedback-based automated release of medication through skin has been reported in the literature [1]; however, the sensing focused on few nonspecific markers (such as pH) that, alone, may be associated with an array of biological processes. We propose building upon this previous work by developing sensors that measure biochemical markers that reflect specific biological phases of wound healing. These sensors may ultimately be used to diagnose wound healing and guide interventions by physicians and/or automated “smart” bandages.

Considering that the same bandage may stay on a wound for a maximum of one week, and that most visible cellular changes in a wound occur on a time scale of 12 hours or more, we planned to develop a strategy that could eventually sample 2-3 biochemical markers every 6 hours for up to one week. The biochemical markers that will be discussed are tumor necrosis factor-alpha (TNF-α), interleukin-6 (IL-6), and albumin. The first two are well-known markers of inflammation, and the last one was chosen as a marker that would peak at a later stage of the wound healing response.

We used an antibody-based approach to sensing because of its proven ability to detect cytokines and chemokines in the relevant sub-picomolar (pM) to nanomolar (nM) biological range. Furthermore, because of the availability of thousands of commercial

antibodies, it is straightforward to optimize and/or scale up to include different and/or a wider range of markers in the future. Some of the main challenges for in vivo use of these sensors are (1) nonspecific binding and fouling of the sensor, and (2) saturation within minutes of exposure to biological fluids, thus precluding dynamic sensing. As will be seen in this report, the sensors were found to be highly specific in biological fluids and when directly applied onto wounds. The antibody-ligand bond is difficult to reverse without using harsh treatments that may damage other sensor components, therefore we used sensors for single measurements only and did not attempt to carry out dynamic sensing or to "regenerate" sensors for multiple measurements. Rather, we developed sensor covers that can be selectively opened. Furthermore, our goal was to demonstrate that sensor arrays can open different sensors at different times to get time series data, with each sensor used only once.

1.3 Choice of Initial Targets for Sensing

Following injury, the wound healing response is known to occur in an orchestrated sequence of stages, namely inflammation, proliferation, and remodeling [2]. We have chosen to monitor inflammation and angiogenesis in the wound. We are targeting these relatively early stages of the wound healing response because it enables early intervention, with the potential of long-term beneficial impact. In addition, the wound has not re-epithelialized yet; thus, transport barriers between the sensors and the wound surface are minimized.

Among the earliest signals released after injury are damage-associated molecular patterns (DAMPs), such as high-mobility group box 1 (HMGB1), which in turn causes the release of multiple pro-inflammatory cytokines from locally recruited neutrophils and macrophages, such as TNF$-\alpha$, and IL-6 [3]. A typical time course following injury will see a sequence starting with HMGB1, followed by TNF$-\alpha$, and IL-6. We selected TNF$-\alpha$ and IL-6 as initial picks for evaluating wound progression through the inflammation phase.

A decrease in pro-inflammatory cytokines along with an increase in pro-resolution cytokines (e.g. IL-10) and growth factors (e.g. stromal-derived factor-1 [SDF-1], vascular endothelial growth factor [VEGF]), signals transitioning of the inflammation phase to the proliferative phase of wound healing. A critical aspect of this phase is the growth of blood vessels into the wound area, which in turn provides the nutrient supply for dermal and epidermal cells to migrate. Reconstitution of a continuous epidermis indicates the end of this phase. Many growth factors and chemokines can be used to monitor this stage of wound healing; however, because angiogenesis is a critical prerequisite to the reconstitution of both the dermis and epidermis, we will monitor one factor that is specifically involved in the development of blood vessels, namely SDF-1.

Biophysical characteristics of the wound are also different from adjacent normal skin. In early stages immediately surrounding the wound area is a zone of hyperemia where blood flow is increased due to inflammation-related vasodilation [4]. This, together with a local increase in metabolic activity from recruited inflammatory cells, causes the local temperature of the wound to increase by 1.1 to 1.2 degree Celsius (°C) (and even more

for infected wounds) compared to intact skin [5]. As wound blood flow is restored, the temperature gradient between wound and surrounding intact skin is expected to vanish. Thus, temperature fluctuations in the wound are likely to occur throughout the wound healing process. This temperature variability factor will likely need to be incorporated into the design of the sensing platform because most biochemical sensors are sensitive to temperature. Furthermore, temperature information may eventually be used as a biophysical marker of the wound stage.

1.4 Choice of Wound Healing Model

Several in vitro (cell culture) and in vivo (animal) models of wound healing are available and widely used. Rodent models (especially mice and rats) are extremely popular since they are relatively inexpensive yet recapitulate many of the complex interactions between post-injury immune response and the damaged tissue layers. Although rodent injuries to skin, in particular, are known to heal mainly by contraction rather than granulation tissue formation as is mostly the case in humans [6], many of the cellular processes that characterize wound healing exist in both, such as inflammation, angiogenesis, cell migration, and cell proliferation. Thus, mouse models of skin excision and burns will be used as a platform to characterize the ability of sensors to measure biochemical changes in the wound. Furthermore, mouse studies will be used to quickly generate data sets that can correlate sensing data to histological information that provides the ground truth on the status of inflammation, angiogenesis, and healing stage of the wound. Although several soluble factors that have known roles in rodent wound healing play a different role or no role in human wound healing [6], we have carefully chosen markers that are known to behave similarly in both species.

2 METHODS, ASSUMPTIONS, AND PROCEDURES

2.1 Nanowell Sensor Design and Basic Operation

Starting with the oxygen plasma treated fused silica substrate, the bottom electrode is defined through lithography process with positive photoresist, and metalized using e-beam evaporation of 100 nm gold on top of 5 nm chromium, which serves as the adhesion enhancing layer. After the successive deposition of multiple metal layers, the bottom electrode is patterned through lift off process. Then, a 40 nm aluminum oxide layer is deposited on the whole wafer using atomic layer deposition at 250°C. The top electrode is fabricated then through the similar lithography, metallization, lift off and atomic layer deposition process, yet with the second mask. After the whole deposition process is completed, two electrodes are formed and share a 20 micrometer (μm) × 20 μm overlapping area at the terminal of each electrode. There is an insulation layer, 40 nm aluminum oxide, gapped two electrodes, and prevent them from short-circuiting. Subsequently, the pattern of nanowells, a 5 × 5 array of 2 μm wells, is created in the overlapping area through lithography with the positive photoresist. A series of wet etching process includes oxide layer etching, gold etching, chromium etching, and the second oxide layer etching, and the cleaning of photoresist was performed in sequence to form the key structure, nanowell of the sensor. The oxide layer on top of the bonding

pads part is also etched to expose the pads for measurements. A fluidic cell with 5 millimeter (mm) diameter well is bonded on top of the sensor chip to confine the reagent, providing a stable measurement environment.

The completed sensor consists of two electrodes opposite to each other, and with a 40 nm insulation layer between. The two electrodes share a 20 μm x 20 μm area with 25 patterned microwells that are each 2 μm in diameter (**Figure 1**). The principle of the sensor for the detection modality is that the impedance across the sensor is continuously monitored, which would change as the binding of target protein occurs.

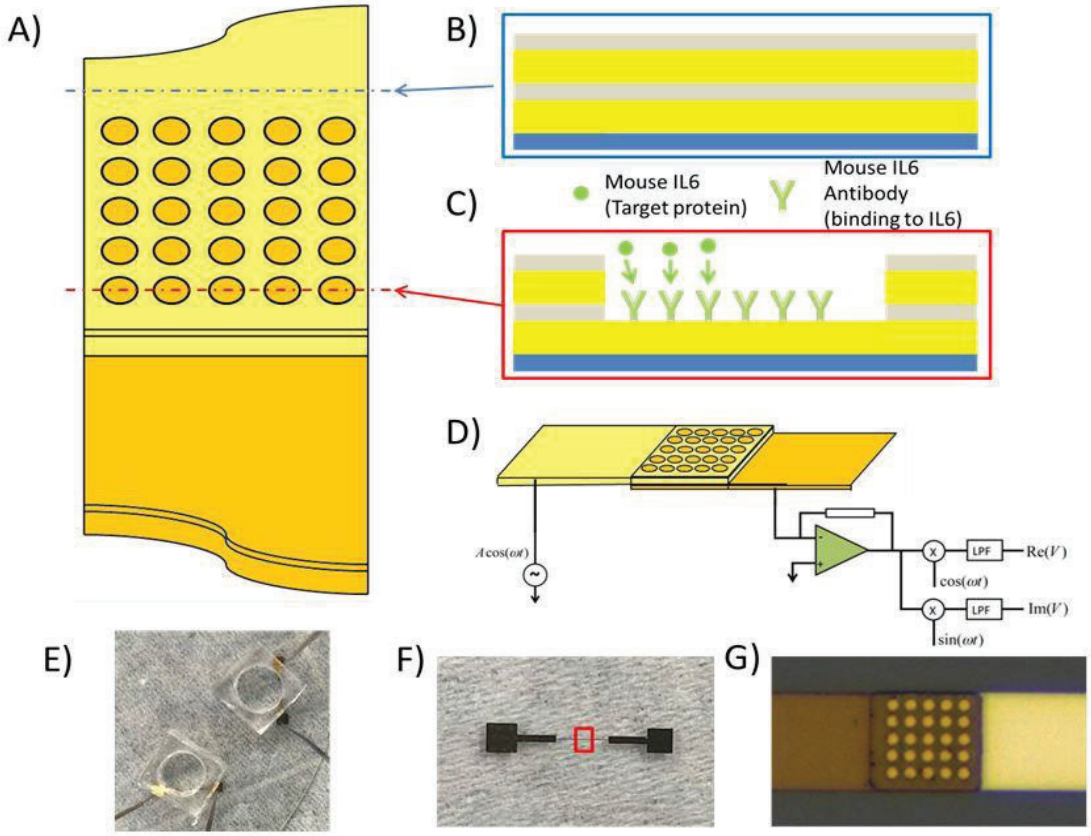

Figure 1: A schematic view of the nanowell sensor. Figure 1B and 1C is the cross-sectional view of the sensor without and with the nanowells. Figure 1C also illustrates the target protein binding to the antibodies which is immobilized on the sensor surface. Figure 1D- G shows the principle of the measurement setup, the photo of the device setup, the photo of the whole sensor, and a zoomed in image of the nanowell.

The dry nanowells are incubated with a solution of antibody in phosphate-buffered saline (PBS), which causes adsorption of the antibody to the well surfaces. Specific binding of the target antigen on the antibody coating increases the protein layer thus impeding ion transfer inside the nanowells, resulting in an impedance increase. The amplitude of the impedance increase is determined by the amount of bound material,

which significantly depends on the target protein concentration in the samples. For taking a measurement, the liquid sample was pipetted onto the nanowell and impedance was measured over time at room temperature, and in some cases on a warm plate at 37.5°C.

A multiplexing circuit was also developed to expand the throughput of the nanowell measurements. The platform consists of a custom designed printed circuit board with a multiplexer (MUX) chip, and an embedded microprocessor (Raspberry PI) to program the control logics. We have utilized the Raspberry Pi 2 Model B for controlling the multiplexing capability in conjunction with multiplexer chips (MAX14611) to switch between 2 nanowell sensors. A custom Printed Circuit Board (PCB) which can be seen in **Figure 2A** was built for interfacing the MAX14611 chips using the Raspberry Pi 2 to the lock-in-amplifier (Zurich Instruments HF2IS Impedance Spectroscope) and the nanowell sensors. Although we have only used one channel of the Impedance spectroscope for this work, the 2 MUX chips on the custom PCB allow for sensors to be connected to both the channels of the Zurich Instruments HF2IS Impedance Spectroscope simultaneously, thus fully utilizing its dual-channel capability. **Figure 2B** shows the data from the system; the data highlighted in blue is from sensor 1 whereas the data highlighted in red is from the 2nd sensor. Error! Reference source not found.**C** shows the decoded data where it has been separated into two separate groups corresponding to the respective sensor output. The working of the PCB is further illustrated in **Figure 2A**. The sensors' 1st terminal is connected to the output of the Zurich Instruments, HF2IS. The 2nd terminal of the sensor is connected to the MUXchip MAX14611, which in turn is connected to the input of the Zurich Instruments, HF2IS. The Raspberry Pi 2 uses the Serial Peripheral Interface (SPI) to control the switching between the sensors using its SPI library. A simple program written in Python is executed on the Pi which switches between sensor 1 and 2 using the SPI bus.

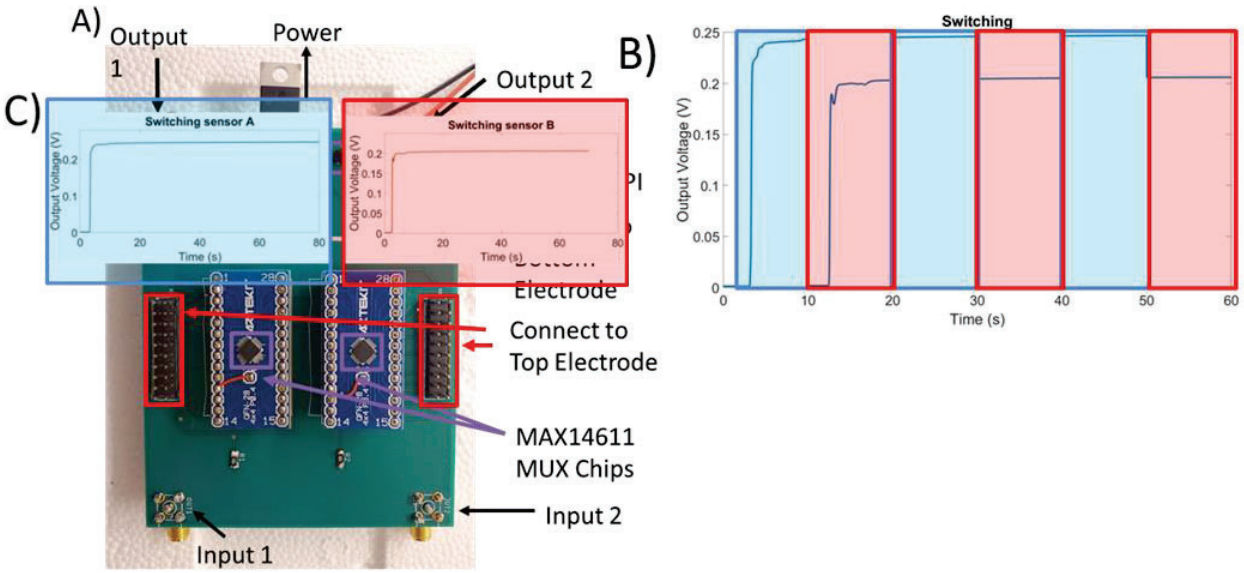

Figure 2: Multiplexing platform photo and diagram. A) The photo of the MUX chip and the circuits. B) Real time data of the output when the PBS was introduced to two sensors. C) Extracted data of the two sensors from the data in panel 2B.

Here, we have demonstrated the capability of our system for multiplexing two sensors, however, the board has been designed to provide multiplexing capability for 16 sensors which may be utilized by making slight modifications to the Python code on the Raspberry Pi and connecting additional sensors to the board.

2.2 Complementary-metal-oxide-semiconductor (CMOS)-chip/nano-well Interface

A CMOS/nano-well cytokine sensing system was built on a flexible PCB with a dimension of 3.7 × 3.2 cm^2 compatible to bandage form factor (**Figure 3**). The CMOS chip integrates the impedance spectroscopy transmitter/receiver system, with low-power and low-noise performance for high sensitivity quantification. The chip is custom designed and fabricated in a 65 nm standard commercial semiconductor foundry process allowing drastic cost reduction [7]. The core of the impedance sensor is based on direct-conversion architecture. As previously shown in **Figure 1C**, the cytokine binding to the nano-well sensor surface with immobilized probe antibody to mouse IL-6 blocks the ion transfer inside the nano-wells, leading to impedance increase from the binding event [8]. To sense this complex impedance change, the CMOS chip excites the sensor at 700 kilohertz (kHz). The sensed current is processed on-chip with integrated trans-impedance amplifier, and then frequency down-converted through in-phase (I) and quadrature (Q) clock to acquire the impedance information [9]. In addition, we implemented four sensing pixels on-chip to allow multiplexing of nano-well sensor array for simultaneous measurement of multiple cytokines (TNF-α, IL-6, etc.).

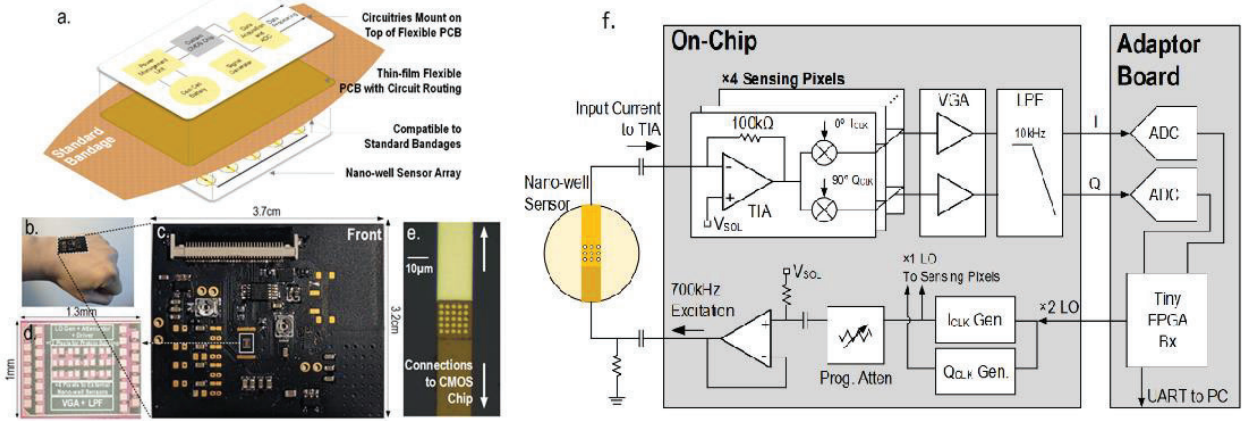

Figure 3: Components of smart bandage. a) & b) Design of CMOS/nanowell hybrid smart bandage c) Flexible PCB with the custom silicon chip d) Micrograph of custom 65nm CMOS e) Microscopic photograph of nano-well sensor f) (below) CMOS direct conversion transmitter/receiver architecture for impedance spectroscopy for label free detection of cytokines in complex wound fluids

A 2nd generation custom designed chip was fabricated, using similar manufacturing methods, to improve noise and gain performance. The architecture is shown in **Figure 4A** below, and the experimental set up for testing is shown in **Figure 4B**.

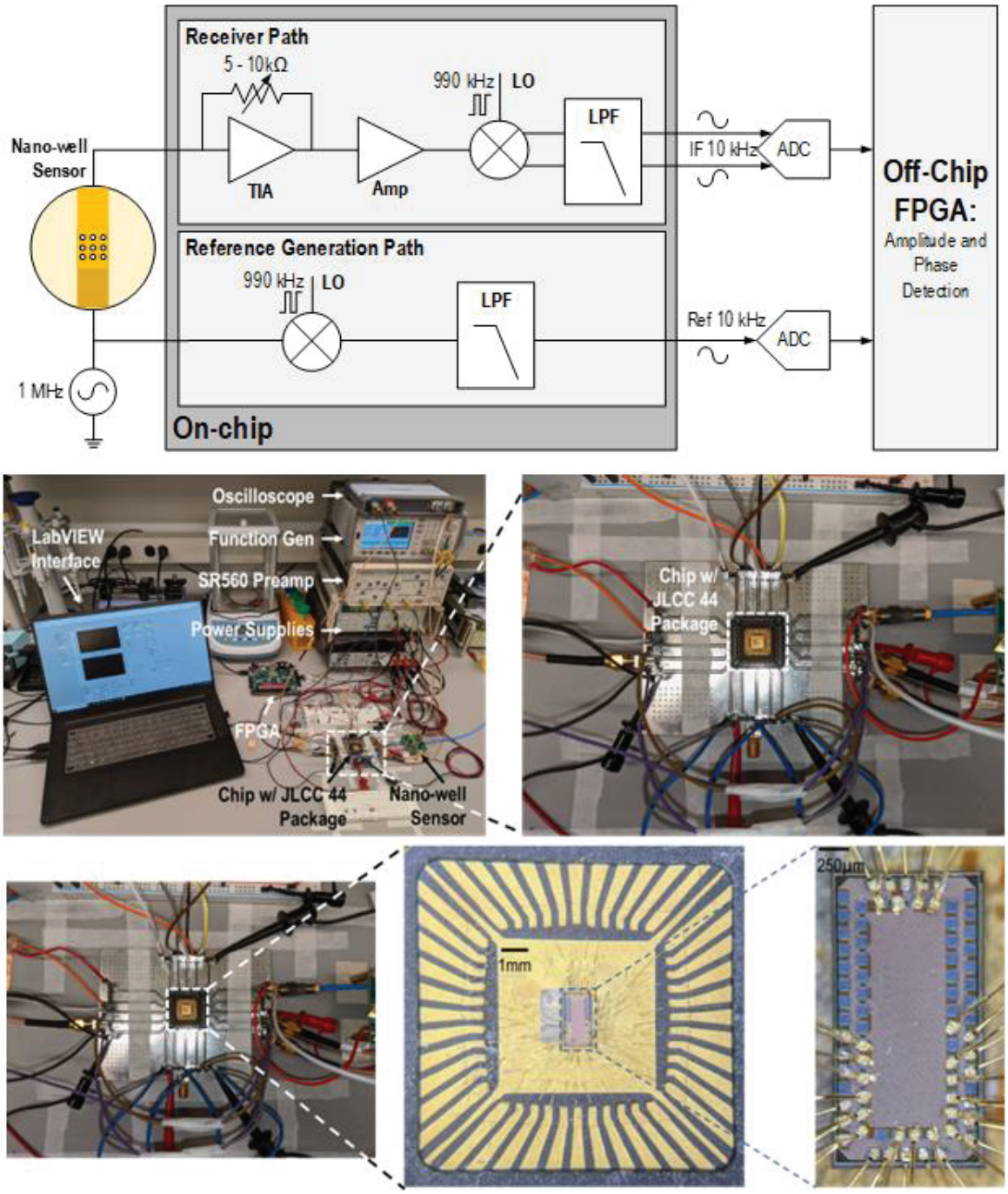

Figure 4: CMOS chip. (A) Circuit design of new CMOS chip. (B) Measurement setup for chip characterization (C) Wirebonding details for CMOS testing.

2.3 Manufacturing and Actuation of Graphene Oxide Nanowell Covers

A PDMS mold was prepared using Sylgard 184 kit (Dow Corning, USA) and different size holes (3, 4, 5 mm) were punched in the mold using a hand punch (**Figure 5 – step**

1). A graphene oxide (GO) solution was obtained from MSE supplies (AZ, USA). Cellulose nitrate (CN) filter papers with 47 mm diameter and 0.8-micron pore size (Whatman, UK) were used for the vacuum filtration process. At the first step, we clamped the CN filter paper in a vacuum filtration setup (Wheaton®, USA) (**Figure 5 – step 2**). Then, we drop casted 2 milliliter (mL) of GO solution on the filter paper and completely filtrated under vacuum. Next, we annealed the filter paper with the deposited GO film at 50 ºC for 30 minutes. We used a hand punch or laser cutter (Universal Laser Systems, USA) to cut different sized GO membranes with a CN backing layer.

The GO membrane was then attached to the PDMS mold using 3M double-sided tape (**Figure 5 – step 3**). First, we fixed the GO+CN membrane to a thick piece of paper using tape. Using the laser cutter, we prepared annular double-sided tapes with openings matching the PDMS mold hole diameters. Using the annular double-sided tape, we peeled the GO membrane from the CN backing layer on thick paper, and then transferred it to the PDMS mold for testing. The PDMS layer with the GO membrane was then placed on a glass slide, and one or several micro-vibration motors (vibrating mini motor disc from Adafruit, USA) were attached to provide vibration to the layer (**Figure 5 – step 4**). For on-demand nanowell sensing tests, instead of a plain glass slide, we placed the PDMS with GO cover and motor on glass coverslip with a nanowell electrochemical sensor patch with a PDMS ring shaped liquid containment zone.

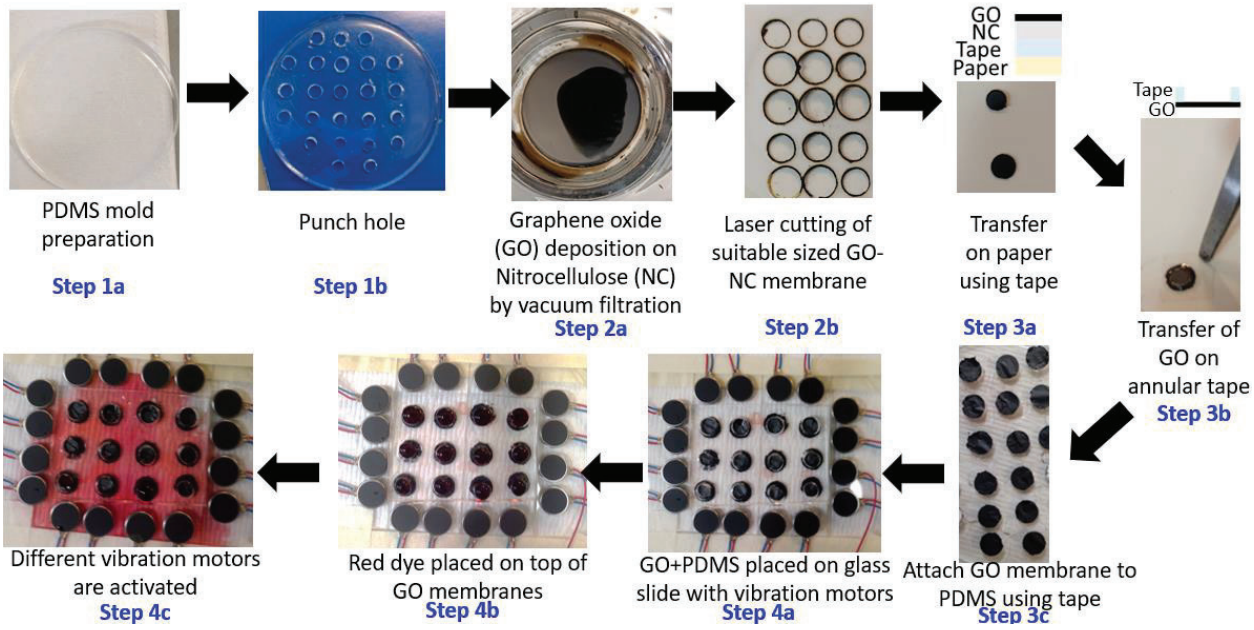

Figure 5: Steps involved in preparation and testing of GO membrane on-demand opening using micro vibration motors.

2.4 Simulation of Vibrating GO Membrane Covers and PDMS Slabs

We performed simulations to determine the eigenfrequency-based resonant modes of vibrating circular GO membrane covers and PDMS slabs (i.e., the substrates/structures holding nanowell sensors and membrane covers). Our initial efforts focused on modeling the membranes. For our models, we used the same material properties for GO during simulation as reported by Liu et al. [10], and we considered the GO membranes in finite element analysis (FEA) using shell elements with no pretension. We also included an added mass to replicate water that might be adjacent to or sitting on the membrane. We performed both time-dependent and frequency-based simulations with vibratory excitation to help us understand if the frequencies of excitation being provided with our actuators were in a similar regime to resonant modes of the membranes. GO membranes with a diameter of a few millimeters and thickness of approximately 10 μm were the focus of our simulations and experiments.

For the simulation of PDMS slabs, the questions involved how material, geometry, and position might affect the amplitude of vibration reaching the membrane covers. For these simulations, the PDMS slabs were a few millimeters thick, 2 cm in width, and 6 cm in length. We designated a domain at one end of the lab as the source of vibration and included four hollowed regions as locations for the membrane covers. This approach allowed us to predict how the amplitude of vibration would vary across the entire device, and thus observe how location might affect the timing of ruptured membranes.

With simulations of the slabs and the membranes, we began to consider how we might couple the simulated responses to predict the amplitude (or acceleration) of vibration applied to membranes across a substrate. We also began to create models that would consider fatigue as the mechanism for rupturing membranes. The reasoning for thinking about using fatigue is that the membranes typically vibrate for more than 10,000 cycles before rupturing. Our systematic approach to modeling the vibratory response includes four phases of simulation/characterization: 1. Defining excitation, geometry, and material properties; 2. Frequency-dependent structural modeling of the substrate/body of the device; 3. Finding the amplitude of vibration at locations along the substrate; 4. Modeling the damage accumulated to predict the breaking of membranes.

2.5 Animal Wound Model and Wound Fluid Collection

Animal studies were approved by the Rutgers Institutional Animal Care and Use Committee (IACUC). Wild-type C57Bl/6 male mice, approximately 10 weeks old (body weight ~25 grams (g)), were purchased from Charles River Laboratories (Wilmington, MA). The mice were anesthetized with isoflurane (Henry Schein, Melville, NY), shaved and naired to expose intact skin. One day later, the day of surgery, the mice were anesthetized, and betadine scrub and 70 percent (%) ethanol were applied alternatively three times to prepare the dorsum for wounding. A full-thickness square incision, 1.5 cm x 1.5 cm in size, was made on the back of the animal. The wound was covered with a Tegaderm semi-permeable transparent dressing that was held in place with a few sutures far from the wound edge. At selected time points, the Tegaderm was removed

and rinsed with 1 mL PBS, which was then stored frozen for later analysis.

Wound fluid samples (from the PBS wash of the Tegaderm) were analyzed offline on the nanowells or via commercial ELISA kits (Invitrogen, Thermo Fisher Scientific), or multiplex immunoassays (Eve Technologies, AB, Canada). In some animals, the nanowell sensors were directly applied onto the wound (for about 10 minutes) at the selected time points. In general, only one in situ in vivo sensing procedure for one specific marker was performed at any given time point. After the measurement, the wound was covered with a new Tegaderm and returned to the housing facility until the next time point.

3 RESULTS AND DISCUSSION

3.1 Nanowell Impedance Response in Diluted Wound Fluid Samples

To begin, nanowell sensors coated with anti-mouse IL-6 were prepared and tested in diluted wound fluid samples. **Figure 6** shows representative data of the sensor response to samples with different IL-6 concentrations. Panel A shows the impedance response as a function of time in a sample containing high levels of IL-6. After addition of the sample, there was a progressive increase in impedance reaching a plateau of 3.5% above baseline after ~10 minutes. Panel B shows the impedance increase with a sample containing a relatively low level of IL-6, which resulted in a similar impedance response but of lower magnitude, reaching only 1.7% above baseline. Panel C shows a negative control response where a mouse sample was placed on top of nanowells pre-coated with anti-human IL-6 antibodies. Because the anti-human IL-6 antibodies do not cross-react with mouse IL-6, there is no anticipated binding of the mouse IL-6 in the nanowell. We observed a transient biphasic response upon addition of the sample with a very slight decrease in impedance (about 0.5% in this case) from baseline.

In order to calibrate the sensor response vs. IL-6 concentration, diluted wound fluid samples from mouse wounds were analyzed with the anti-mouse IL-6-coated nanowells and the same samples were analyzed using a standard mouse IL-6 ELISA kit. The plateau level of the impedance curve recorded for each nanowell measurement was used here, and correlated with the concentration of IL-6 determined by ELISA. The correlation between impedance and IL-6 concentration is shown in **Figure 7**. A simple nonlinear equation can be used to accurately represent the sigmoidal shape over a range covering nearly 3 orders of magnitude. Another set of wound fluid samples was analyzed using the nanowells and the same equation was used to convert impedance values into concentrations. These concentrations are plotted vs. concentrations measured by ELISA in the same samples in **Figure 8**, which shows that both techniques yield very similar results. This indicates that the techniques are nearly identical in terms of sensitivity, precision and dynamic range.

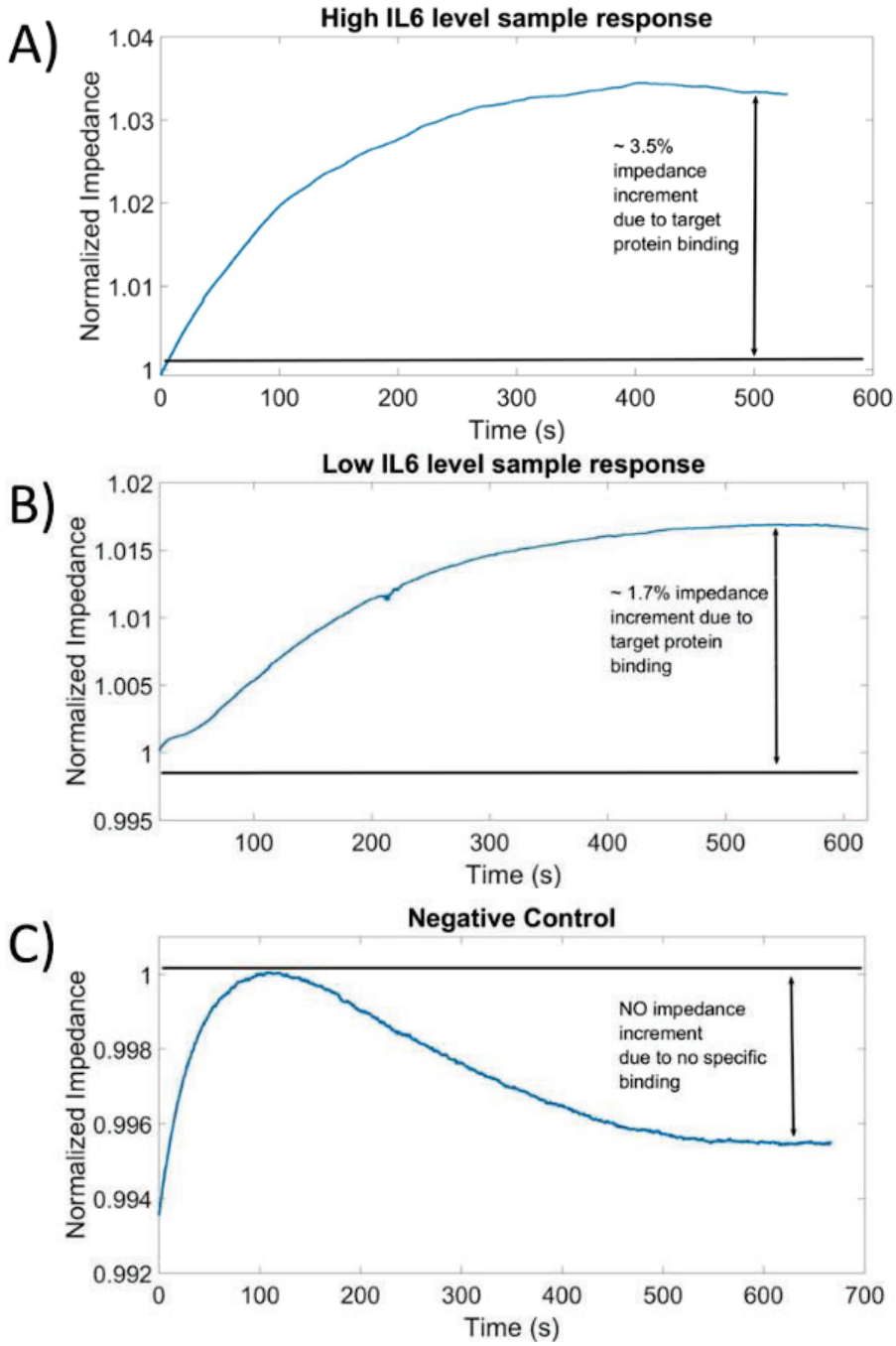

Figure 6: Real-time normalized impedance change of anti-IL6 coated nanowells to different samples. A) Mouse wound fluid sample with high IL-6 concentration. B) Mouse wound fluid sample with low IL-6 concentration. C) Mouse wound fluid sample dispensed in a well coated with non-crossreactive anti-human IL-6 antibody (negative control).

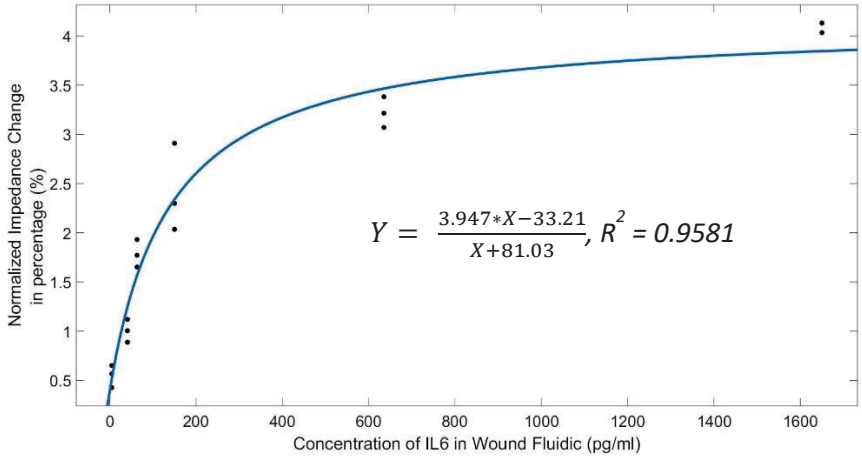

Figure 7: Nanowell sensor response to different wound fluid samples as a function of IL-6 concentration in those samples, for values ranging from single pg/ml to thousands pg/ml. Each sample was measured 3 times with the nanowell sensors.

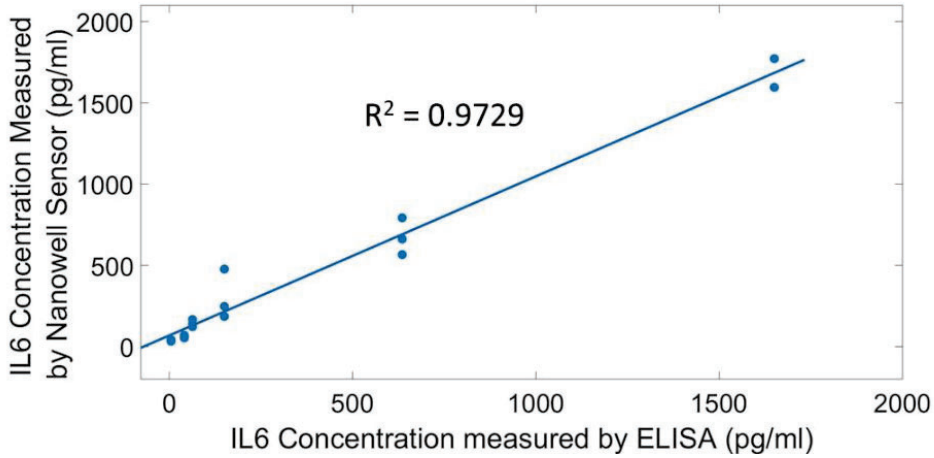

Figure 8: Comparison and correlation between nanowell sensing and ELISA for IL-6. Mouse wound fluid samples were analyzed for IL-6 using both methods (nanowells in triplicate) and the correlation is shown relative to the y=x line.

The same procedure, and same mouse wound fluid samples were used to measure TNF-α in nanowells and by ELISA. For this purpose, the nanowells were coated with anti-mouse TNF-α antibodies, and **Figure 9** shows the impedance response as a function of TNF-α concentration. Again, a nonlinear fit equation was used to model the entire range; note that the concentration range of the wound fluid samples for TNF-α was slightly less than 2 orders of magnitude and therefore a linear scale was used to represent the horizontal axis. Correlation between concentrations determined by nanowells vs. by ELISA is shown in **Figure 10**. As was the case for IL-6, the correspondence between both methods is excellent overall.

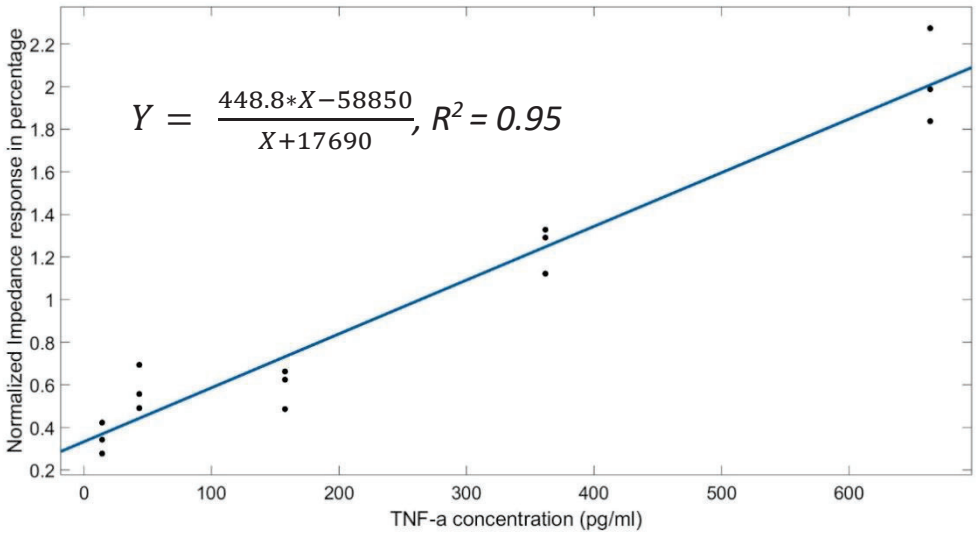

Figure 9: Nanowell sensor response to different wound fluid samples as a function of TNF-α concentration in those samples, for values ranging from ~10 to 800 pg/ml. Each sample was measured 3 times with the nanowell sensors.

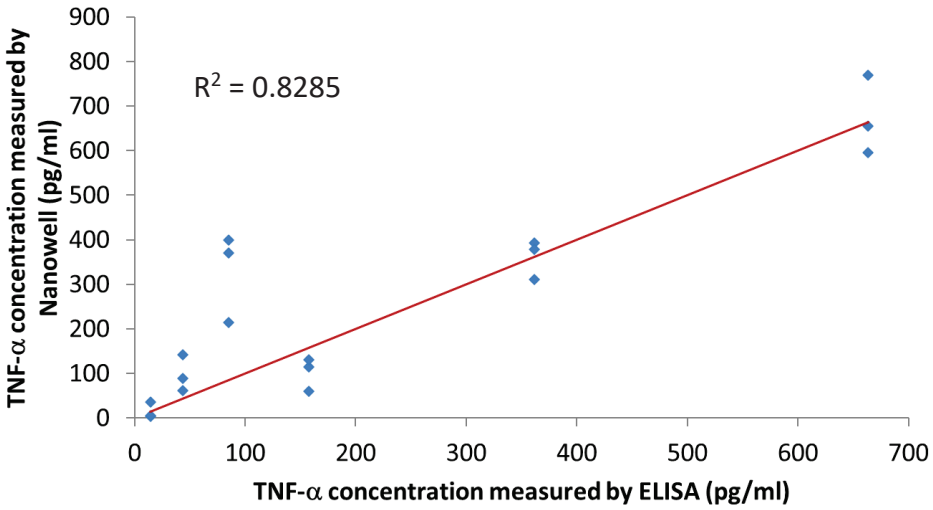

Figure 10: Correlation between nanowell vs. ELISA determination of TNF−α concentration.

We did notice in some instances a discrepancy between the two methods with certain wound fluid samples. To ensure that this was not experimental error, we repeated the measurements with both techniques. An example of such a case is shown in **Figure 11** below, where both methods yielded different results. It is important to note that although both the ELISA and the nanowell sensors use antibodies to detect the target protein, the ELISA is a commercial product and the manufacturer does not share the details of the antibodies used. The antibody used in the nanowell sensor is different and likely recognizes a different epitope on TNF-α. In the proteolytic environment of the wound fluid, it is possible that peptide fragments from the degradation of TNF-α molecules are

picked up differently by both assays. This would require further investigation using a panel of anti-TNF-α antibodies and analysis of the TNF-α degradation products using mass spectrometry, which was well beyond the scope of this project.

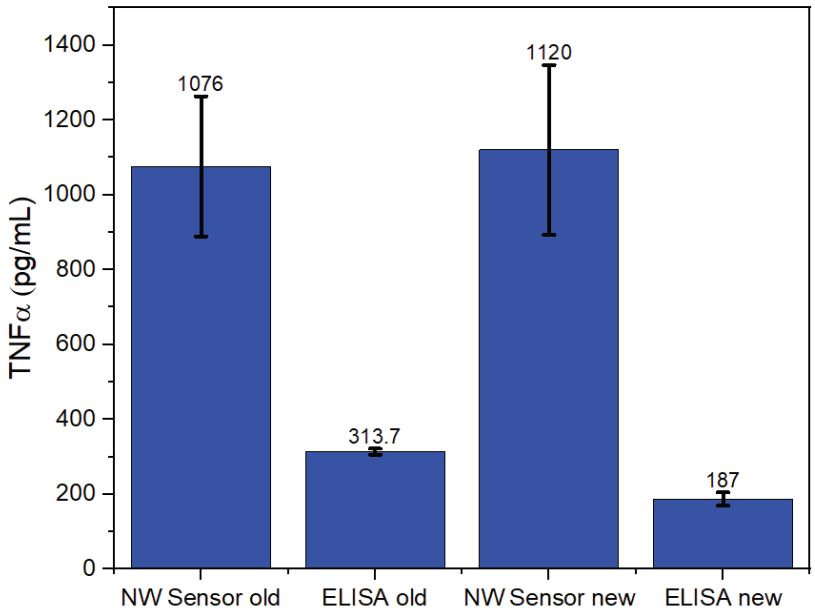

Figure 11: Comparison of nanowell (NW) and ELISA results for a specific wound fluid sample that showed a discrepancy. The original measurements ("old") were repeated ("new"), yielding the same results.

3.2 Effect of Temperature on Nanowell Impedance Response

As we move towards implementing physiological conditions to our measurements, we investigated the impact of measurement temperature. Using PBS on the sensor, the temperature was increased from 22°C (room temperature) to 37.5°C (body temperature). The sensor baseline impedance shifted downward as the temperature increased (**Figure 12A**). A wound fluid sample was measured in parallel at room temperature and at 37.5°C on nanowells coated with anti-IL-6. The raw data for the triplicate measurements at each temperature were collected and analyzed as usual, using the plateau value of the impedance response, and the summary of the results, shown in **Figure 12B**, suggests that the impedance rise due to IL-6 was virtually identical at room temperature and at 37.5°C.

Taken together, these results show that while the baseline impedance value of the nanowells was affected by temperature, the differential rise of impedance due to antigen bainding was very similar at both temperatures. Thus, moving forward, in an in vivo measurement context where multiple nanowells may be applied onto the wound, some nanowells should be used specifically to record baseline values at the same time as the other nanowells are used to measure the target antigen, so that the differential response can be obtained.

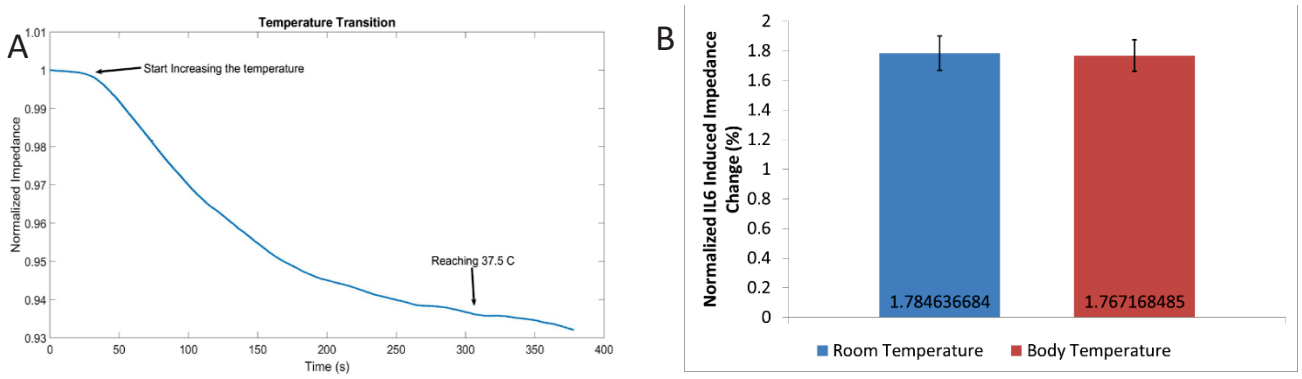

Figure 12: Effect of temperature on nanowell behavior. (A) Effect of rising sensor temperature from room temperature (~22°C) to body temperature (~37.5°C) on sensor impedance in presence of PBS, thus showing baseline values. (B) Impedance change of IL-6 sensor in response to wound fluid sample measured at room temperature vs. body temperature. Values shown are averages of triplicate measurements.

3.3 Mouse Wound Levels of IL-6 and TNF-α

We tested the ability of the nanowell sensors to measure cytokine levels (TNF-α and IL-6) in wounds in situ. For this purpose, C57Bl/6 male mice (about 25 g body weight) were subjected to a 1.5 cm x 1.5 cm excisional wound on the dorsum. The wound was full-thickness; in other words it extended all the way into the panniculus carnosus and therefore the entire dermis and epidermis were removed. The wounds were covered by a Tegaderm dressing to prevent dehydration. The sensors were pre-coated with an antibody to TNF–α or IL-6, and then applied onto the wound. The mouse was anesthetized and laying on the ventral side, with the wound facing up. Thus, the sensor had to be placed upside down onto the wound (**Figure 13**).

Figure 13: Positioning of the nanowell sensor on a mouse wound.

An impedance response was observed in reaction to the presence of mouse IL-6 in the wound in situ, which was different from that observed using an anti-human IL-6 antibody. The anti-human antibody does not cross-react with the anti-mouse antibody,

and thus represents the baseline response (**Figure 14**). Thus the nanowell sensors appeared to function similarly when applied directly to the wound as they would when liquid samples are added onto them on the laboratory bench.

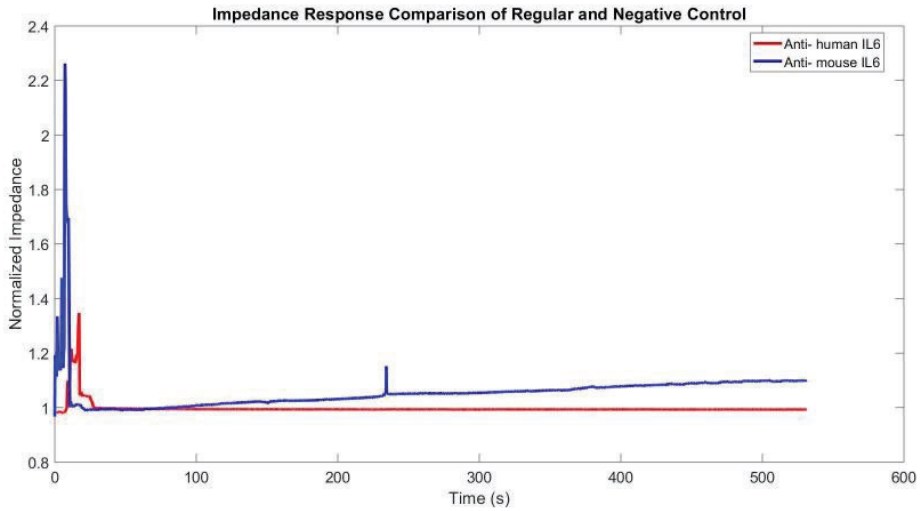

Figure 14: Comparison of the impedance when a mouse wound is contacted with a sensor coated with anti-human IL-6 (red line) vs. a sensor that is coated with anti-mouse IL-6 (blue line). The difference corresponds to the impact on impedance of specific binding of mouse IL-6 present in the wound.

In a subsequent study a cohort of 5 mice, cytokine levels were measured in situ at the following times post wounding: 10 minutes (shown as “day 0” on the graphs below), 1 day, 3 days, 7 days, 10 days, and 14 days. Two mice were used for TNF–α, and 3 mice were used for IL-6 measurements. **Figure 15** displays the gross morphology showing the evolution of the wounds on individual mice; after 14 days, the wounds had nearly closed.

Nanowell impedance measurements on the wounds were converted into concentrations based on the correlation curves described previously in **Figure 7** and **Figure 9**. Both TNF–α and IL-6 showed a similar dynamics in the mouse wounds, increasing to a peak at day 3 post-wounding, to decrease afterwards up to day 10 (**Figure 16A**). Measurements could not be taken at day 14 because the wounds were dry and nearly closed. Comparing these dynamics to that of the wound closure process, one can see that day 3 corresponds to the very beginning of the wound contraction process (**Figure 16B**).

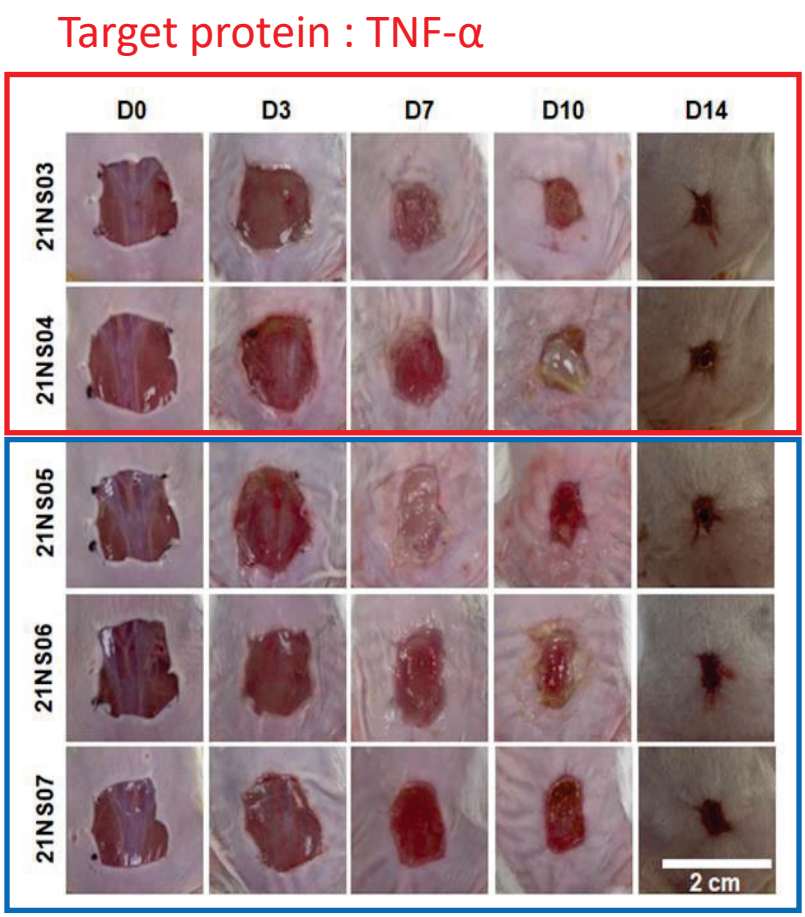

Figure 15: Wound appearance up to 4 days after injury. Wounds were normally covered with Tegaderm, but the dressing was removed to take the picture and perform the cytokine sensing.

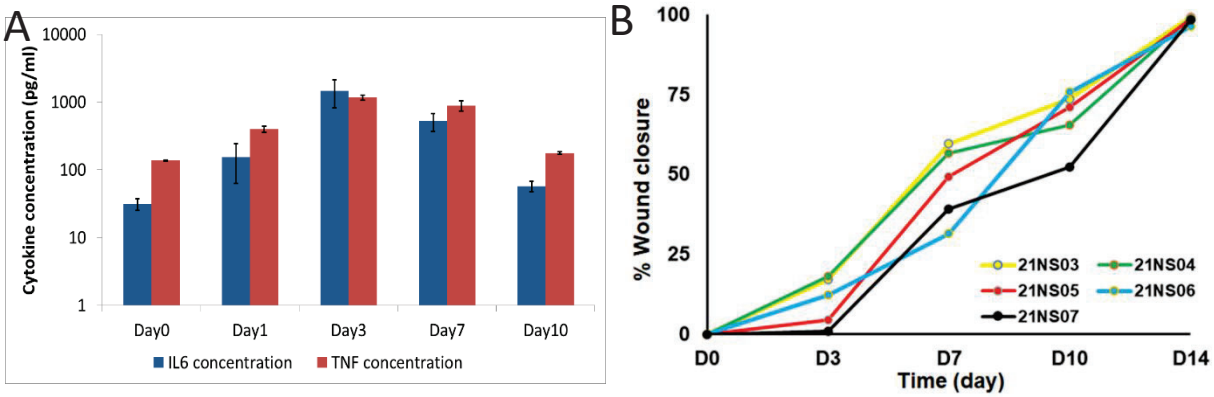

Figure 16: Time correlation between cytokine levels detected in situ (Panel A) and wound closure dynamics (Panel B; derived from quantification of images in **Figure 15:** Wound appearance up to 4 days after injury. Wounds were normally covered with Tegaderm, but the dressing was removed to take the picture and perform the cytokine sensing.). The peak of cytokines was seen on post-wounding day 3,

which is the point where the wound begins to undergo rapid closure via contraction. Day 0 corresponds to approximately 10 minutes post wounding. Note that TNF–α values are an average of N=2 mice, and IL-6 values are an average of N=3 mice.

Diluted wound fluid samples from the same animals were analyzed ex vivo using the nanowells, and the data are shown in **Figure 17** below. The general dynamic behavior is similar to that observed with the direct in situ measurements for both IL-6 and TNF–α measurements, with a peak value at 3 days post injury.

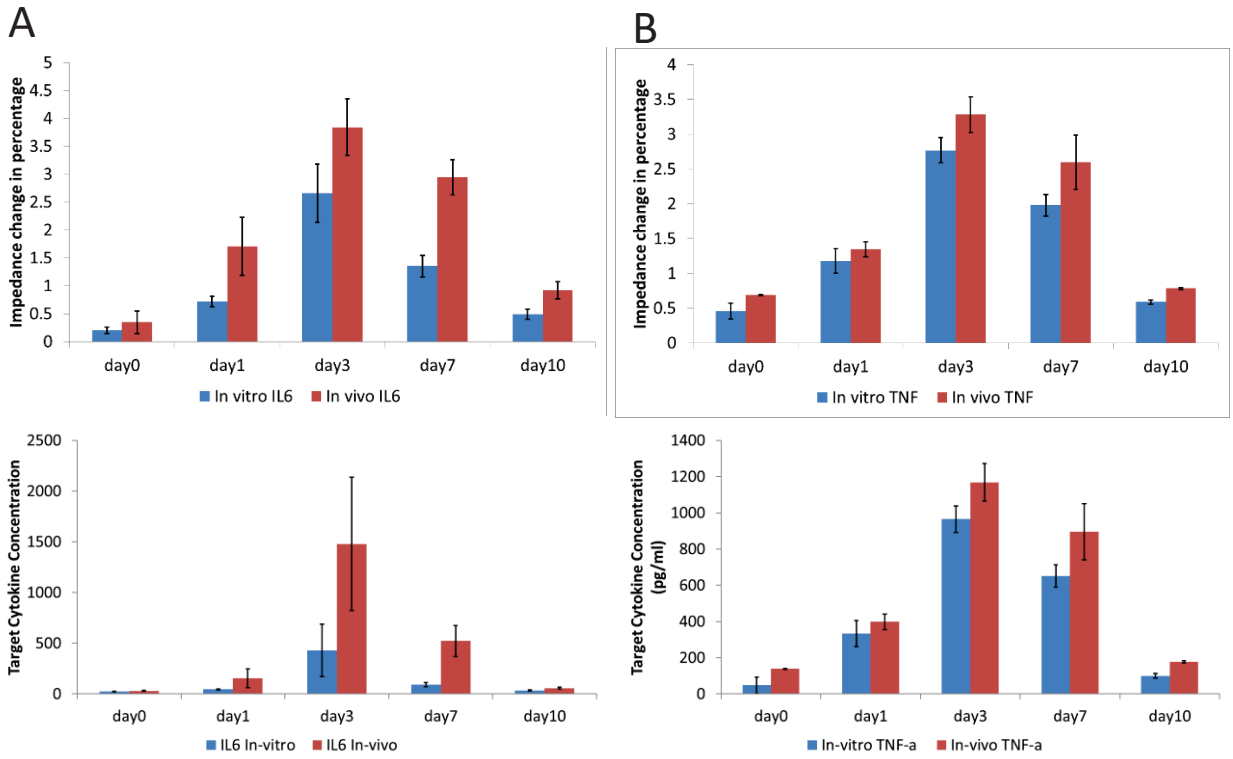

Figure 17: Raw Impedance values and calculated concentrations of cytokines measured in vitro (wound fluid samples) and in vivo (on the wound themselves). (A) IL-6 data (B) TNF–α. Data from 3 animals for IL-6, and 2 animals for TNF–α. These data are from the 5 animals reported in **Figure 15**. Nanowells were used to determine the concentrations.

3.4 Identification of Albumin as Post-Inflammation Phase Marker

TNF–α and IL-6 measured in diluted wound fluid ex vivo and in situ on mouse wounds both showed a peak on day 3 post-wounding and are expected to reflect the inflammation phase of wound healing. We attempted to find a third marker to measure that would show a different dynamic, one that would peak later and would reflect transition to the proliferative phase (post-inflammation) of wound healing. For this purpose, we analyzed the same diluted wound fluid samples using a multiplex assay that measured a total of 29 different growth factors and chemokines, several of which are

expected to be involved in angiogenesis and fibrosis.

The data for the markers that were detectable in all samples (14 markers total) is shown in

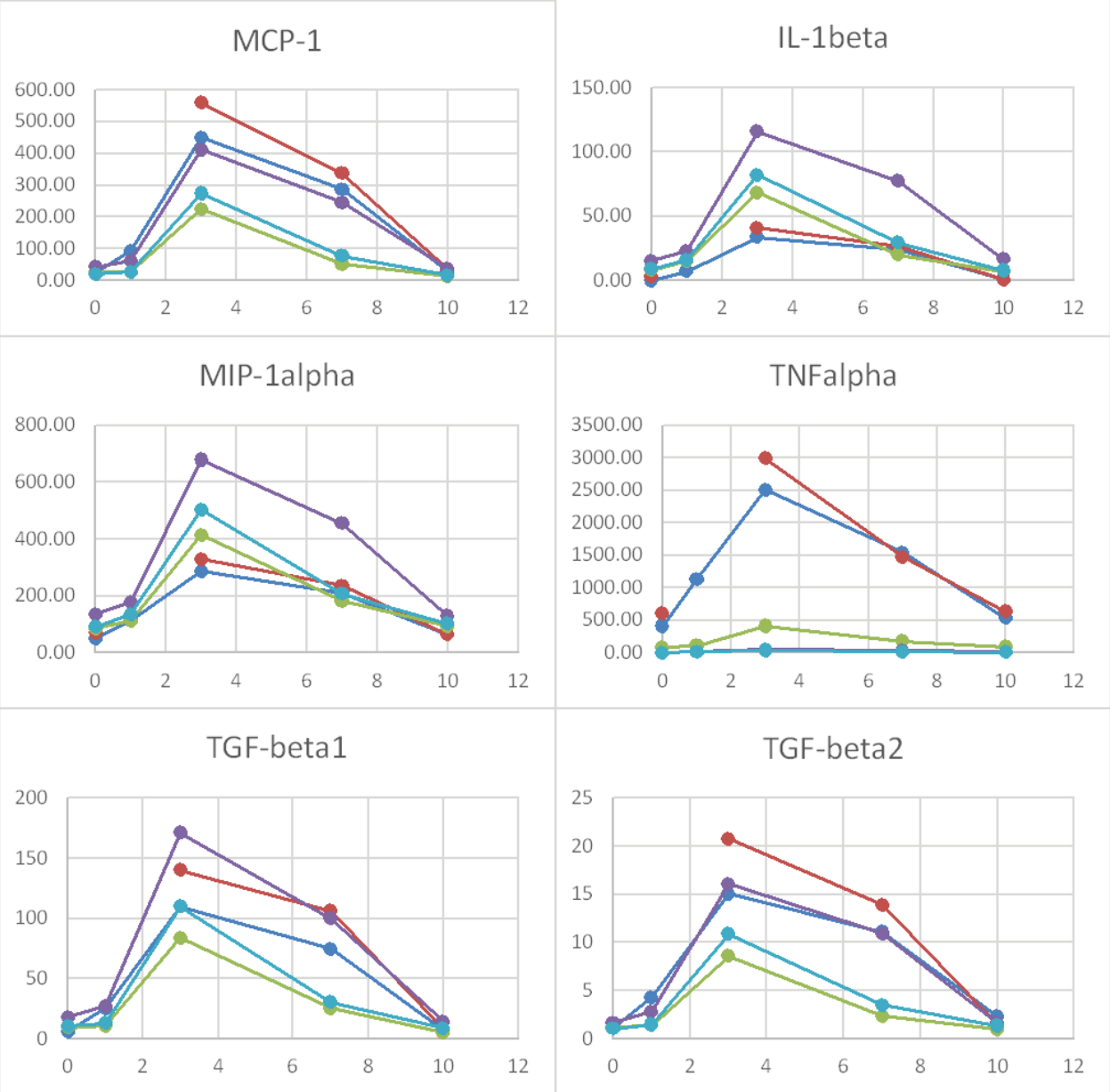

Figure 18 below. Markers that were detectable in only some of the samples were not included. All markers show similar dynamics with a peak value at 3 days. The only exception is SDF-1, which was found to be close to the detection limit in all samples (per discussion with the assay operator), with no clear time-dependent variation. Thus, this approach did not allow us to identify late-stage markers.

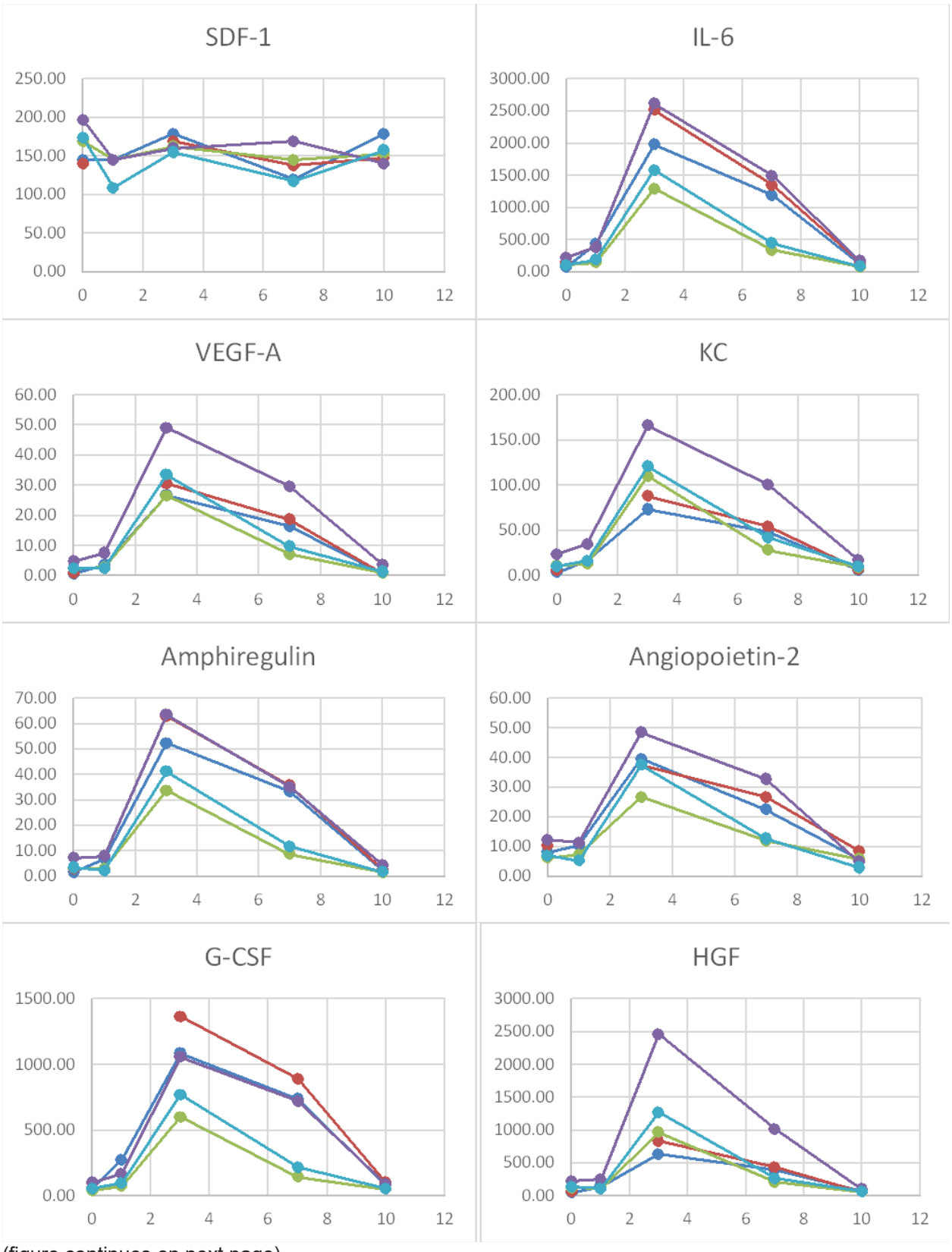

(figure continues on next page)

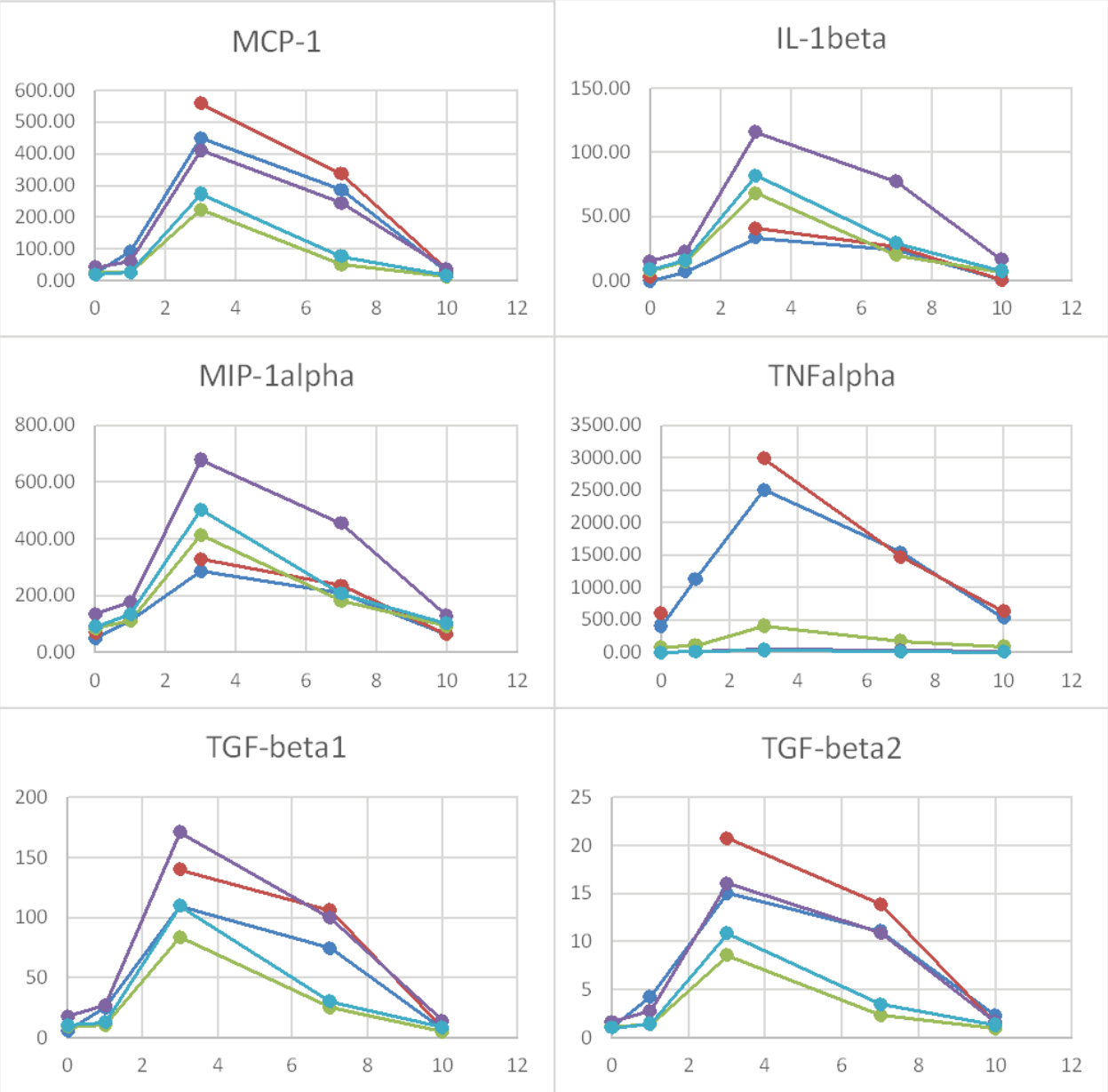

Figure 18: Cytokine/growth factor levels measured on post-injury days 0 (10 minutes post injury), 1, 3, 7, and 10. These wounds had closed by day 14. Lines of different colors represent individual animals. Sample for red group, day 1, was missing, hence the break in the red data curves.

These results prompted us to adopt a different strategy to pursue a 3rd marker with the nanowells. It is plausible that the 3-day peak may reflect an increase in wound fluid production at that time, which would result in more wound fluid content in the diluted wound fluid samples. It is good to remember that those wound fluid samples were collected from bandages removed from the animals, which were then rinsed with a fixed amount of PBS (1 mL). Thus, wounds producing more fluid exudate could likely have more concentrated samples. Hypothetically, if on day 3 wounds produce a lot of fluid, the levels of wound factors will be higher in those samples. In order to “normalize” for wound fluid content, we opted to measure albumin concentration in the samples next. Albumin

is not produced by the wound but rather comes exclusively from the vasculature, which becomes leaky during inflammation. It is therefore reasonable to assume that albumin content is a reflection of how much wound fluid was collected in individual samples.

Nanowells were coated with anti-mouse albumin antibodies and mouse albumin standards (ranging from 100 to 4000 pg/mL) were run in nanowells. As in the case of TNF–α and IL-6, impedance increased vs. time to reach a plateau. The plateau value was used thus yielding an impedance response vs. albumin concentration curve (**Figure 19**).

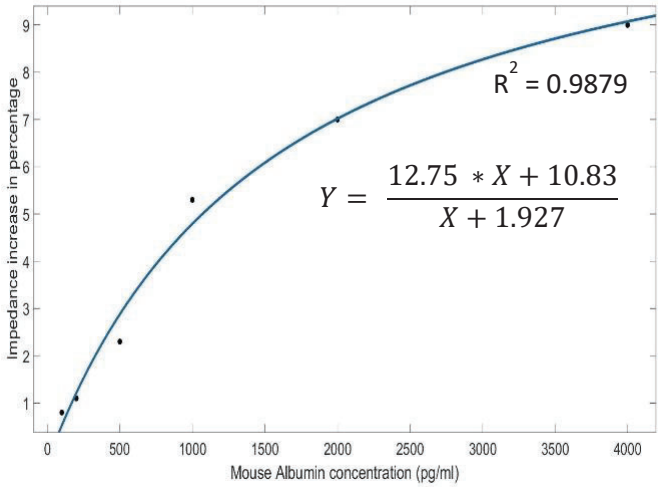

Figure 19: Impedance response in nanowells as a function of albumin concentration.

The anti-albumin coated nanowells were then used to measure the concentration of albumin in the diluted mouse wound fluid samples. Because the samples contained albumin levels that were too high, they had to be diluted by a factor of 1:20x10^6 in order to bring the levels down to the low ng/mL range or below. Results show that albumin peaked at post injury days 7 and 10 (**Figure 20A**), which was an unexpected result. On the one hand, the peak occurs in the late stage of the wound healing response, and thus albumin may be useful as a marker for the post-inflammatory and proliferative phase of wound healing. On the other hand, the mechanism leading to higher levels in the wound in the late stage of healing is unclear. It is plausible that the increased vascularization at this point may provide a higher surface area for albumin extravasation, but this would have to be explored further. The same samples were also analyzed by ELISA, and nanowell vs. ELISA concentration determinations were in excellent agreement (**Figure 20B**), consistent with previous findings with the TNF–α and IL-6 sensing nanowells.

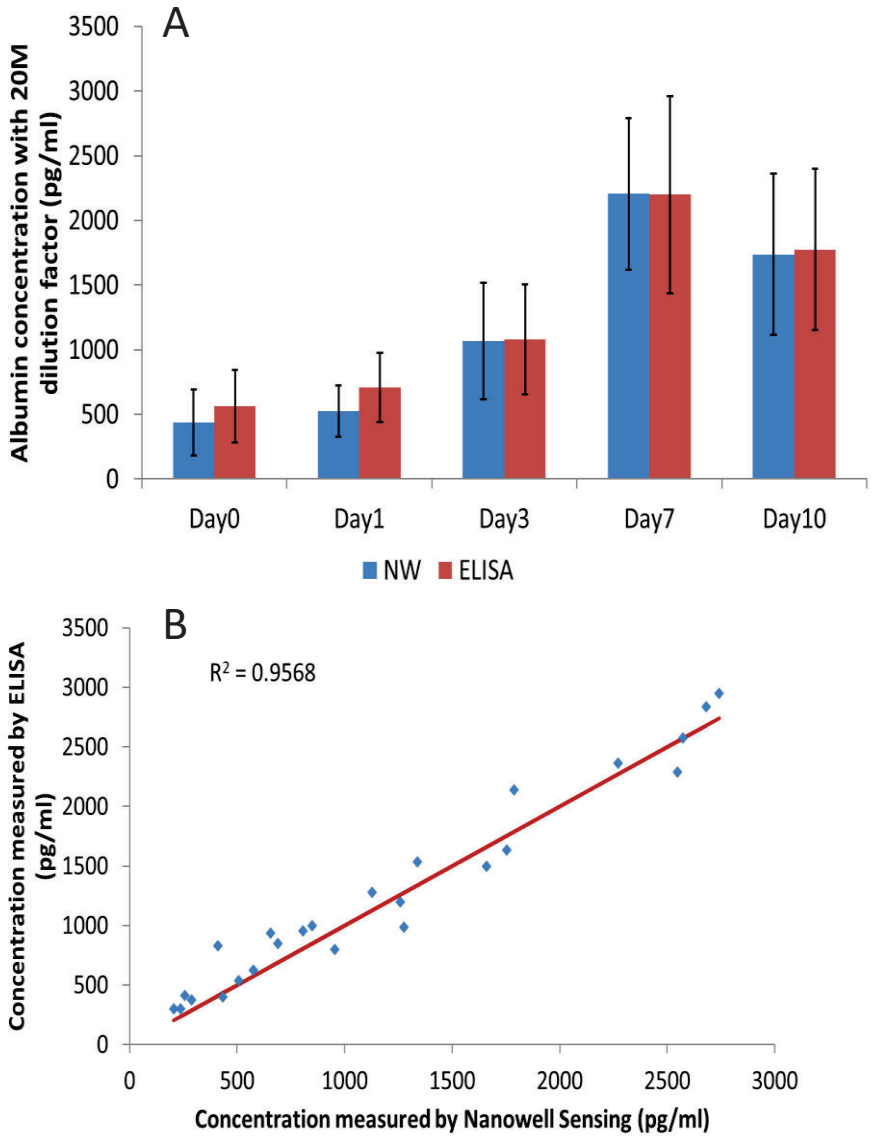

Figure 20: Albumin levels in mouse wound fluid. (A) Albumin levels measured in diluted mouse wound fluid samples from animals shown in Figure 15, using nanowells (NW) and ELISA. (B) Correlation between ELISA and nanowell concentration determinations for albumin.

3.5 CMOS Interface for Multiplexing and Bandage Integration

While accurate measurements of impedance using nanowell sensors was demonstrated with a benchtop Zurich impedance analyzer, realizing further miniaturization of the impedance sensor in a form suitable for a smart bandage requires miniaturization of sensing circuitries. As previously shown in **Figure 3**, the first generation of circuit was based on a direct conversion impedance sensing architecture, where the in-phase and quadrature signal of the current were converted to a DC analog output. Although this approach consumes low power, it suffers from 1/f noise at the DC output.

The second generation of the chip, previously shown in **Figure 4**, solves the issue of 1/f noise by introducing a heterodyne architecture, where a local oscillator (LO) frequency of 990 kHz is deployed to down-convert the 1 megahertz (MHz) excitation to a 10 kHz output frequency. The 10 kHz output frequency is chosen such that the noise performance is optimized between 1/f analog circuit noise and the ADC quantization noise. The second version of the chip has four TIA input pads allowing multiplexing of current inputs from the nanowells.

To characterize the impedance chip performance, two parameters need to be summarized: linearity and noise, where each parameter determines the largest and minimum detectable signal value. From these two values, the system dynamic range can be acquired. **Figure 21** demonstrates the linearity measurement of the chip. The measurement was performed by gradually increasing the input current to the TIA, while the output voltage (V) of the chip can be plotted, until a 1decibel (dB) of drop in amplitude was observed from the ideal linear gain. The value was measured at 175 microamperes (μA). On the other hand, the noise performance was characterized under the largest gain setting of 100 kiloohm (kΩ) (10 kΩ TIA gain and 10 times amplifier gain) with LO frequency set to 990 kHz. Using this setting, the measured noise is summarized in **Figure 21** showing roughly ***20 and 63 pArms*** of input-referred current noise ***at 10 and 100 Hertz (Hz) of bandwidth respectively***.

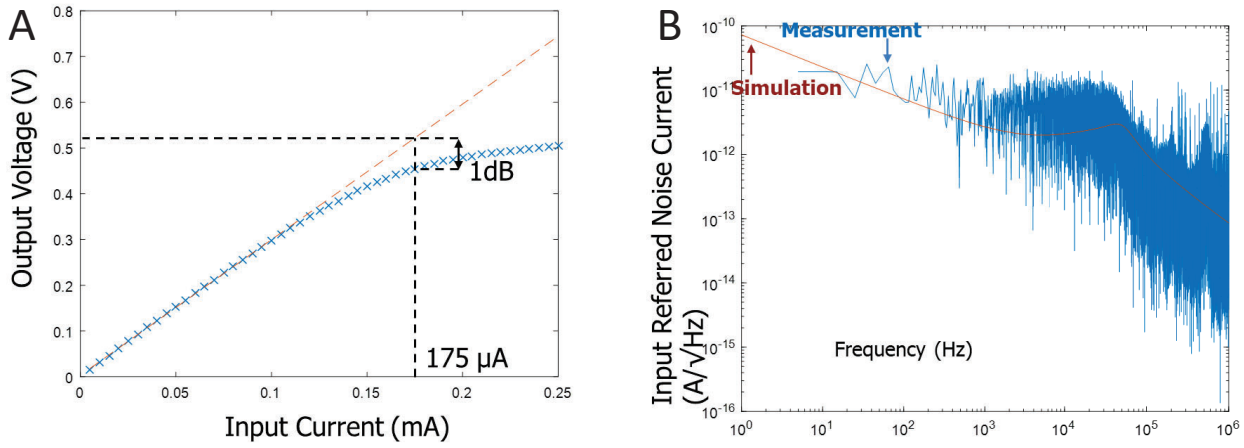

Figure 21: Chip linearity and noise characterization. (A) Chip linearity performance characterization: as the input current increases the output voltage increases linearly. The maximum allowable input current is defined by the output voltage is 1dB lower than the linearized trend line. (B) Chip noise performance characterization that defines the minimum detectable signal. The reported input referred current noise is measured at around 20 and 63 pArms at 10 and 100 Hz of bandwidth respectively. The reported noise is about 15 times less than the previous chip.

The overall chip performance is summarized in **Figure 22**. In summary, compare to the first generation of impedance chip, the new design shows better linearity and noise performance. Overall, the chip shows 44 dB increase in dynamic range compare to the first-generation chip based on direction conversion architecture.

Largest detectable signal:

- **More than 10X Larger than previous**

Smallest detectable signal:

- **More than 10X smaller than previous**

In total **44dB** dynamic range improvement

Parameters	Current Chip	Previous Chip
1-dB Compression	**175 µA**	16 µA
Noise (measured @ 10Hz Bandwidth)	**20 pArms**	300 pArms
Dynamic Range	**139 dB**	95 dB

Figure 22: Performance comparison between the new proposed (heterodyne architecture) and previous chip (direct conversion architecture) showing nearly 44 dB improvements in dynamic range.

Figure 23 shows an example of impedance measurement against time after mouse IL-6 anti-body is added to the nanowell sensor. The measurement shows an average impedance change of roughly 5% across four different trials. Noise performance is also measured with a real wound fluid sample is shown in **Figure 23**. At steady state, the real-time impedance plot shows a 0.02% noise. This translates to roughly 1 ohm (Ω) when the baseline solution is around 6 kΩ. This result shows sufficient sensitivity of the system to detect IL-6 cytokine concentration that is on the order of 100 pg/mL or lower.

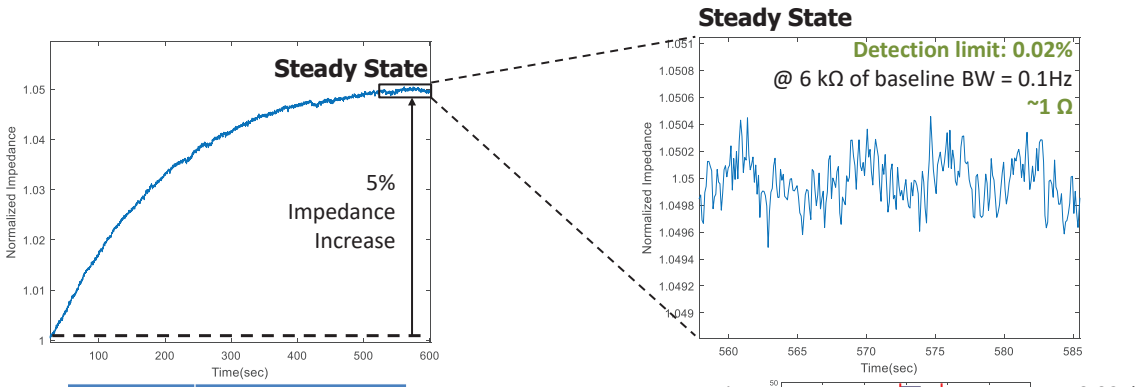

Antibody	% Impedance Change
Trial 1	5.04%
Trial 2	4.34%
Trial 3	5.82%
Trial 4	5.95%

Figure 23: Impedance response variability. (Left) Real-time normalized impedance change using the new chip system with antibody added to the nanowell sensor, showing consistent impedance variations across different trials. (Right) A zoomed in view of the noise performance of the waveform, showing a noise of 0.02%, this corresponds to roughly 1Ω of detection limit with around 6kΩ of impedance baseline.

Then, the wound fluid from mice was collected from different days post-injury and added to the nanowell sensor that was pre-coated with antibody. **Figure 24(left)** shows the real-time impedance waveform against time, for both the old CMOS (top left) and the new CMOS (bottom left). Note that the noise level with the new CMOS is considerably lower, as discussed earlier. The new CMOS data show impedance changes of 2.4%, 1.5% and 1.1% for mouse wound fluid collected from post-injury days 3, 7, and 10 respectively. The same measurements were repeated four times for samples collected from each day and the data are summarized in **Figure 24(right)**. When comparing against prior measurements performed using the benchtop Zurich instrument, the new CMOS+nanowell sensing system shows similar percentage variation.

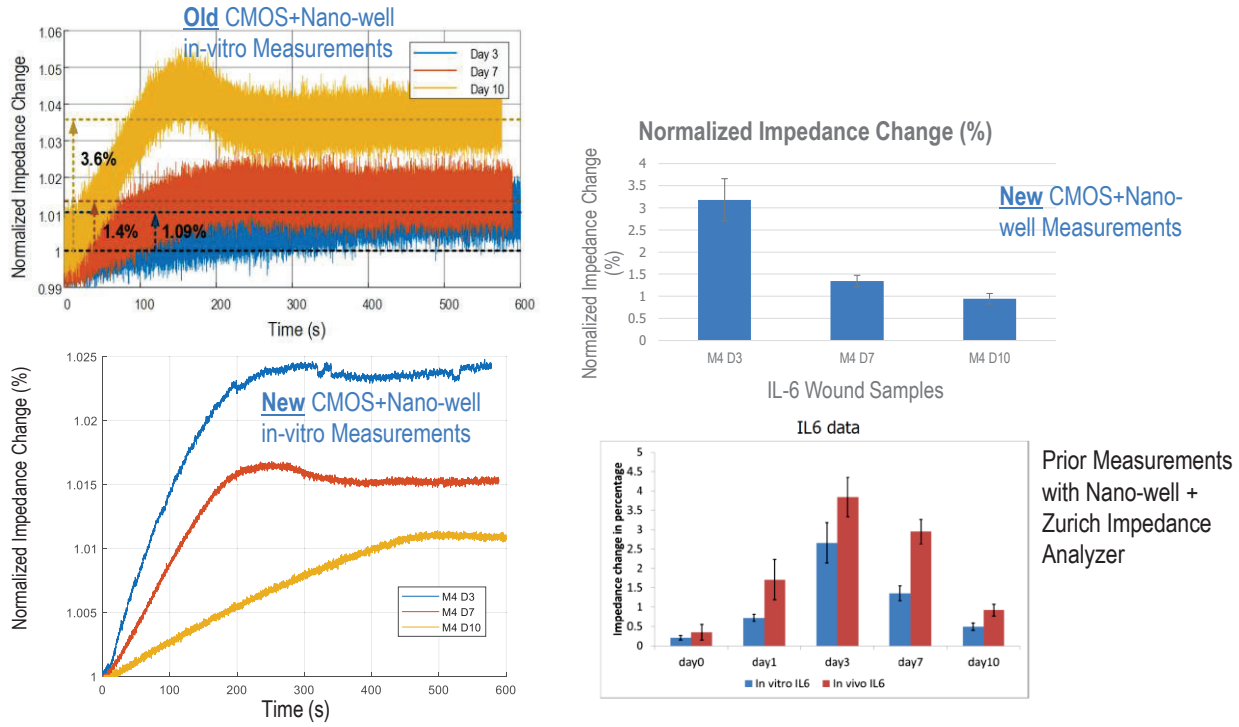

Figure 24: Impedance response to various wound fluid samples. (Left) Real-time normalized impedance change when a sample of mouse wound fluid is added to the nanowell sensor (precoated with anti-IL-6 antibody). The top plot shows typical impedance curves obtained with the ***old CMOS*** and bottom plot shows impedance curves acquired with ***new CMOS***. Note that samples from two different mice were used in each case, thus the means are not directly comparable; however, the noise level is dramatically lower with the new CMOS. (Right) Top figure shows the statistical summary of four trials measured from collected mouse wound fluids using the new CMOS+nanowell setup, demonstrating a close trend (for days 3, 7, and 10) compared to prior measurements performed on the same samples using the Zurich impedance analyzer.

Finally, the measurement results from one particular wound fluid sample (post-injury day 3) are summarized and compared to a standard ELISA test. **Figure 25A** shows the normalized impedance change from the mouse wound fluid samples with varying IL-6 concentration. Correlation between the ELISA and nanowell results is plotted in **Figure 25B** as well. The plot shows high correlation factor between the CMOS+nanowell

sensing system and the ELISA test (R^2 = 0.927), demonstrating the reliability of the new proposed system.

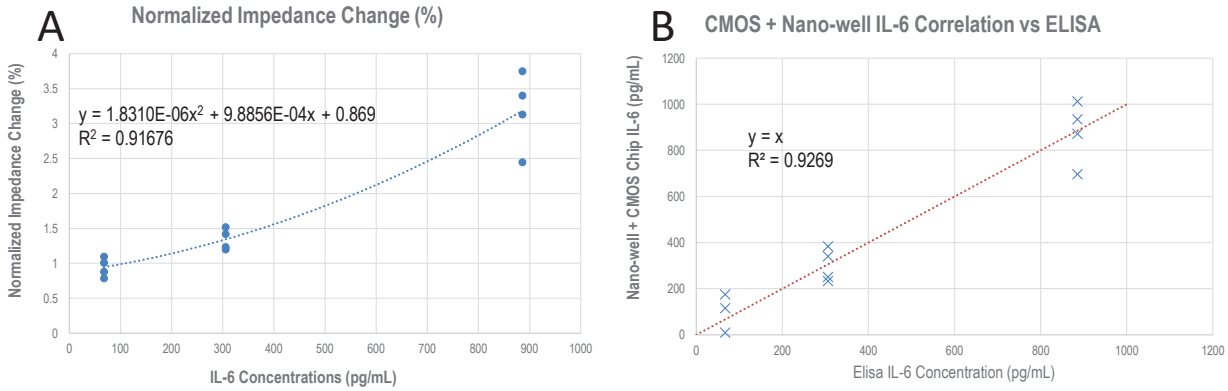

Figure 25: Impedance vs. concentration response. (A) Normalized impedance change against IL-6 concentration in pg/mL, showing the best-fit line and R^2 value of 0.917. (B) Correlation plot of the IL-6 using CMOS+Nanowell setup compared against ELISA from the same mouse wound fluid sample, demonstrating a high correlation factor between the two (R^2 = 0.927).

3.6 GO Membrane Cover Opening and On-Demand Cytokine Measurement

We analyzed GO membrane topography using scanning electron microscopy (SEM). The SEM image of the GO membrane surface shows mostly flat topography with some non-uniformities due to individual GO sheets sticking out (**Figure 26A**). The wrinkles on the surface of the GO membrane are similar to that observed by others with a surface sensitive Everhart-Thornley detector (ETD) [11]. The membrane edge (**Figure 26B**) shows layer by layer stacking of the GO sheet leading to the formation of ~10-μm thick GO membrane (also confirmed by measurement using calipers). Other researchers have also confirmed the layer-by-layer microstructure resulting after the evaporation of water, induced in our case by vacuum and baking [12].

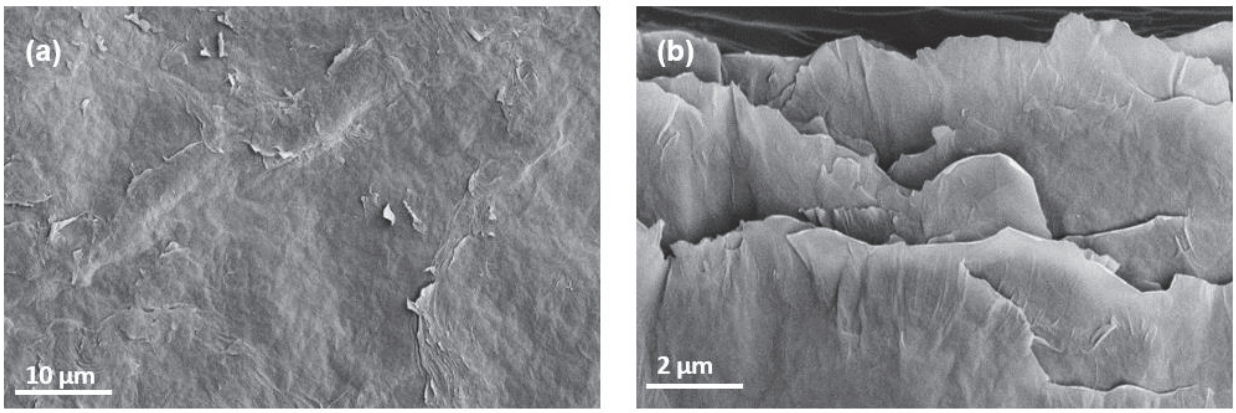

Figure 26: Scanning electron microscopy image of (a) middle and (b) edge of the GO membrane.

Next, we analyzed the GO membrane and micro-vibration motor combination for on-demand sensing. The GO membrane attached to PDMS well is placed on the sensor with PDMS liquid containment ring (**Figure 27A**). The vibration motor was attached to one end of the PDMS well. We placed analyte (300 microliters (μL)) on the GO membrane using a pipette. The nanowell sensor was connected to the impedance analyzer, and after ~2 minutes, the vibration motor was turned on. Two different analytes were used for this sensing test, namely mouse wound fluid in PBS and pure PBS.

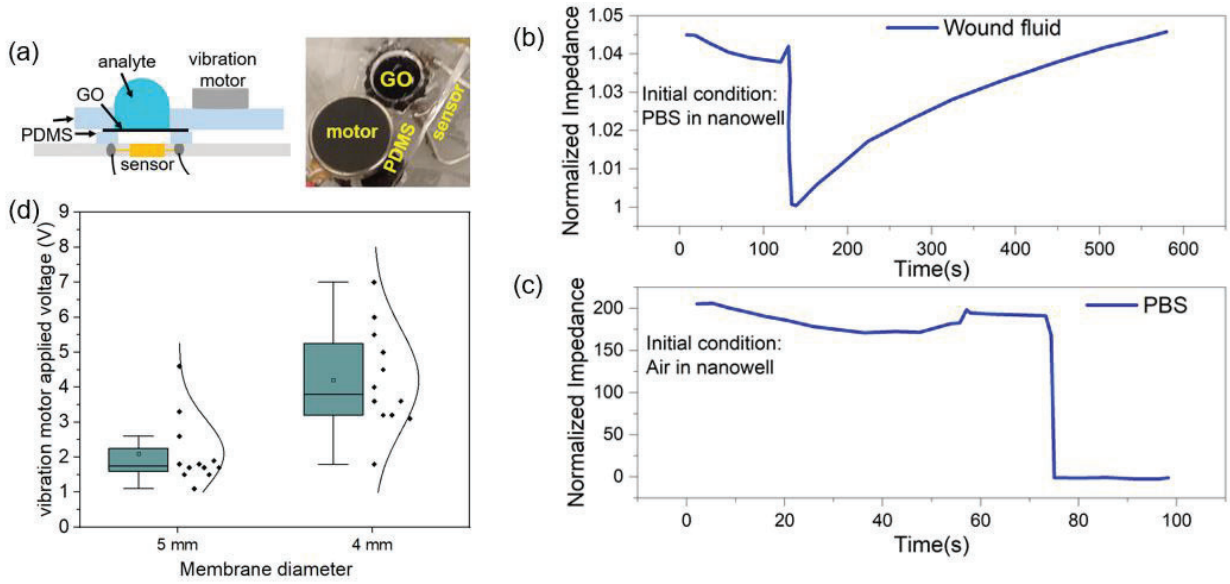

Figure 27: Vibration-induced GO membrane opening for a single cover. (a) Schematic diagram and picture of the setup used to test GO membrane as on-demand sensor cover. (b) On-demand sensing test with mouse wound fluid. (c) Control test with PBS. (d) GO membrane opening power requirement as a function of membrane diameter.

When the analyte was wound fluid, the nanowell sensor was initially partially filled with PBS, and the starting impedance level was relatively low due to the presence of ions in the partially filled sensor nanochannel. As the vibration motor was activated (~100 seconds (s)), there was a sharp drop in impedance, indicating breakage of the GO membrane and the introduction of wound fluid in PBS completely filling the nanochannel (**Figure 27B**). Once the cytokine from wound fluid started to interact with the sensor at the bottom of the well, the impedance increased again (**Figure 27B**). To ensure that the increase in impedance was due to the interaction of wound fluid cytokines with the sensor, a control experiment was performed using pure PBS as the analyte. In this case, the nanowell sensor was empty (or filled with air) to begin with and had a very high impedance (**Figure 27C**). Once the motor was activated (~80 s), the GO membrane broke causing the sensor to fill with PBS, thus resulting in a dramatic reduction of impedance. However, since there was no antigen to bind the sensor, the impedance remained low thereafter. Thus, the GO cover was able to seal the sensor away from the test sample until it was opened by vibration, and vibration did not seem to affect sensor performance.

We also performed additional tests to demonstrate the ability to selectively open GO membranes based on their diameter. **Figure 27D** shows that if the membrane diameter changes from 5 mm to 4 mm, the required vibration motor power (i.e., the applied voltage) changes from ~2 Volts (V) to ~3.5 V on average. Since the motor vibration frequency changes based on applied voltage, our original hypothesis was that the resonant frequency of different diameter membranes likely gets matched with motor vibration frequency at different voltages, leading to membrane breakage/failure at that voltage.

In an effort to develop a system whereby a series of wells can be opened in a prescribed order using a single vibration motor, we designed a PDMS slab containing 3 wells located 1 cm apart along a single axis as shown in **Figure 28A**. The micro-vibration motor was embedded on one edge (at location P0) and the input voltage applied was gradually increased. Movement amplitude of the slab at the location of the motor (P0) and the 3 wells (P1, P2, P3) was measured with an Omron Z4M-W40RA laser displacement sensor. As this happened, frequency increased as well, although after 1.5 volts the frequency began to plateau reaching only slightly over 100 Hz (**Figure 28B**). Interestingly, voltage changed amplitude differentially in different well locations (**Figure 28C**). Thus, frequency applied was in fact lower than the resonance frequency of the membranes, yet breaking was observed in different locations above 1.5 V. Based on these observations, and the fact that cover opening took seconds to minutes, we changed our hypothesis for membrane opening to a damage accumulation fatigue-based model. The theoretical foundation for understanding the process of membrane breaking as a function of amplitude and number of cycles is in the next section.

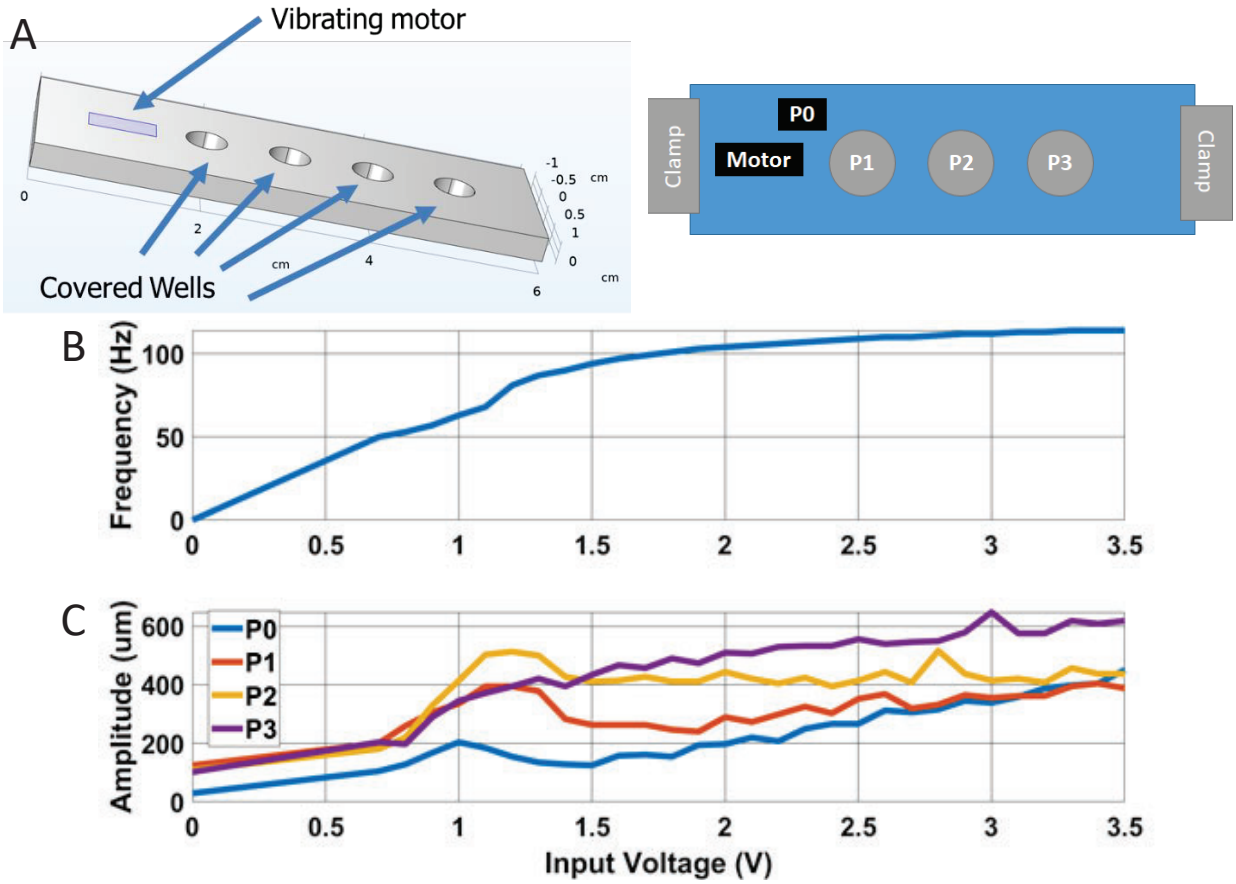

Figure 28: Characterization of vibration of a PDMS slab with a micro vibration motor embedded on one side. Movement was measured using an Omron Z4M-W40RA laser displacement sensor. (A) Geometry of PDMS slab and key locations for measurements. Motor reference location is P0, and well locations are at 1 cm increments from the motor (P1-3). (B) Frequency of vibration by input voltage. (C) Amplitude of vibration at reference locations.

3.7 Theoretical Simulation of GO Membrane Cover Opening

To shed more light on the GO membrane opening mechanism, and ways to control it both temporally and spatially, we performed finite element simulations using COMSOL Multiphysics analysis, solver and simulator software for circular GO membranes. Eigen frequencies found from COMSOL for GO membrane with different diameters and thickness were compared with analytical results to determine the accuracy of initial simulations (**Figure 29**: GO membrane resonance prediction. (a) Eigenfrequency calculation of GO membranes using COMSOL, and (b) table showing a comparison between eigenfrequencies obtained by using analytical formula and COMSOL.). Less than 3% error was found between simulation and analytical results.

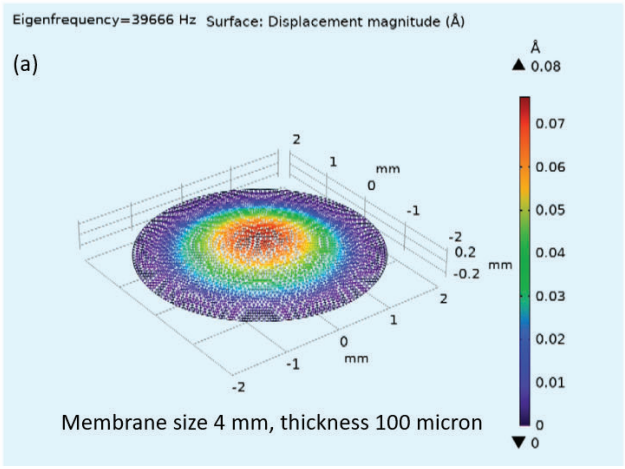

(b)

$$\text{Natural Frequency, } f_{ij} = \frac{\lambda_{ij}^2}{2\pi a^2}\sqrt{\frac{Eh^3}{12\gamma(1-\nu^2)}}$$

Material	Diameter(mm)	Thickness(μm)	Analytical	COMSOL	%Error
GO	4	10	2037.97	2036.3	0.08
GO	4	100	20379.71	20225	0.76
GO	5	100	13043.01	12976	0.51
GO	3	100	36230.59	35771	1.27
GO	4	200	40759.41	39666	2.68
Nickel	4	100	58467.66	58104	0.62

Figure 29: GO membrane resonance prediction. (a) Eigenfrequency calculation of GO membranes using COMSOL, and (b) table showing a comparison between eigenfrequencies obtained by using analytical formula and COMSOL.

Therefore, we moved ahead with the same simulation framework to determine the stress developed on different diameter GO membrane, with the same thickness (10 μm) and 2 mm added water mass on top (since the membrane is in contact liquid during operation) but experiencing 10 millinewton (mN) cyclic load applied at different frequencies. If we assumed there were no viscous damping (losses) in the material, we saw that stress would gradually increase when the load was applied at the resonant frequency of the membrane (**Figure 30**). Therefore, for a 4-mm diameter membrane, when applied load frequency was 193 Hz (resonant frequency of this membrane with added mass) stress increased gradually; whereas when it was 123 Hz, stress developed remained minimal (**Figure 30A**). The same scenario was observed for a 5 mm diameter membrane (resonant frequency 123 Hz) (**Figure 30B**). This matches with the experimental findings, where the 5 mm membrane broke at ~2 V (motor vibration frequency 127 Hz) and the 4 mm membrane broke at ~3.5 V (motor vibration frequency ~155 Hz). This opened the possibility of having a sensor array with different diameter membranes on top, which could be opened selectively using the same vibration source, giving spatial and temporal control.

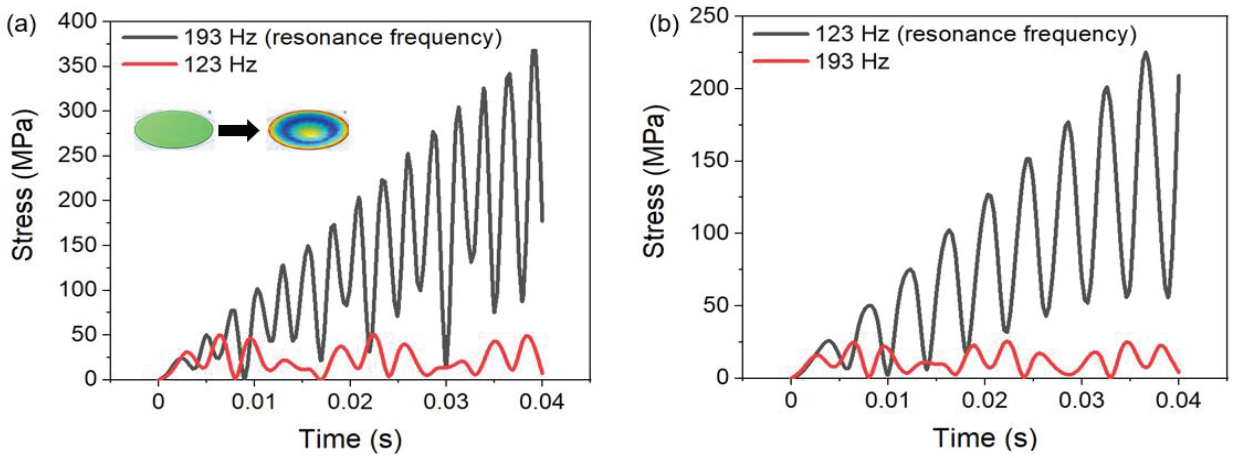

Figure 30: Analysis of stress development due to the application of 10 mN cyclic load on the edge of a clamped membrane having a diameter of (a) 4 mm (b) 5 mm.

The stress does not continue to grow over 10's of cycles because the materials have loss moduli. Going further in our simulations, we moved away from time-dependent simulations and focused on frequency-dependent simulations that depicted steady-state modal responses. As described in Section 2.4, we also focused on two sets of simulations: simulations of the membranes and simulations of the device/substrate. **Figure 31:** Defining the location and type of source of excitation (vibrating motor), geometry of the membrane and overall structure with its holes, and the material properties for the simulations. shows the first phase in our systematic approach of defining excitation, geometry, and material properties.

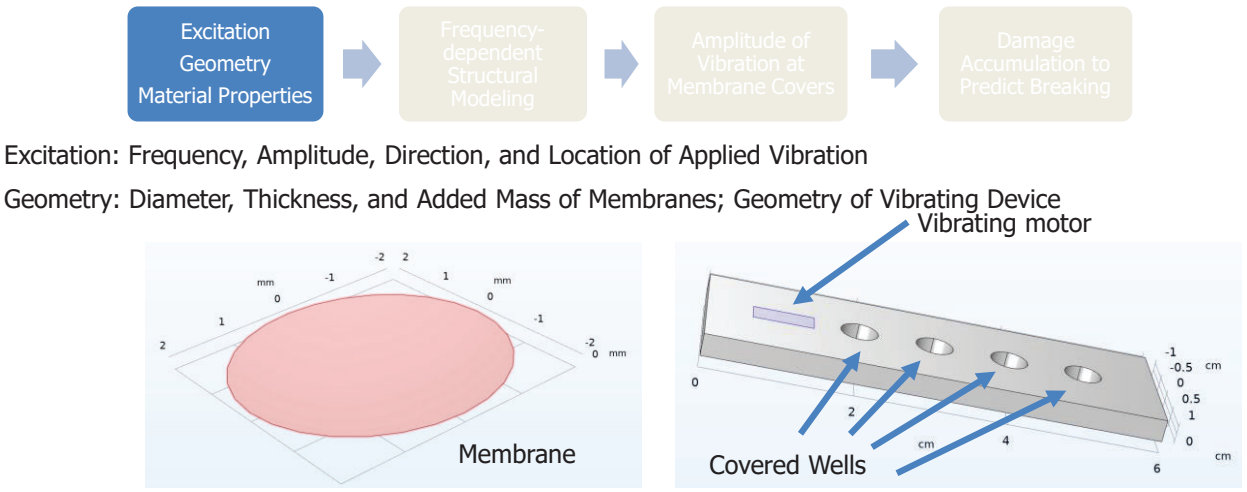

Figure 31: Defining the location and type of source of excitation (vibrating motor), geometry of the membrane and overall structure with its holes, and the material properties for the simulations.

The second phase (shown in **Figure 32**) involved simulating the overall structure of the substrate/device to determine the distribution of acceleration at selected locations. While there are still unresolved discrepancies between the modeling and laser-based measurements of vibratory amplitude measured at selected locations, the simulations and experiments demonstrated that amplitude of vibration was dependent on location.

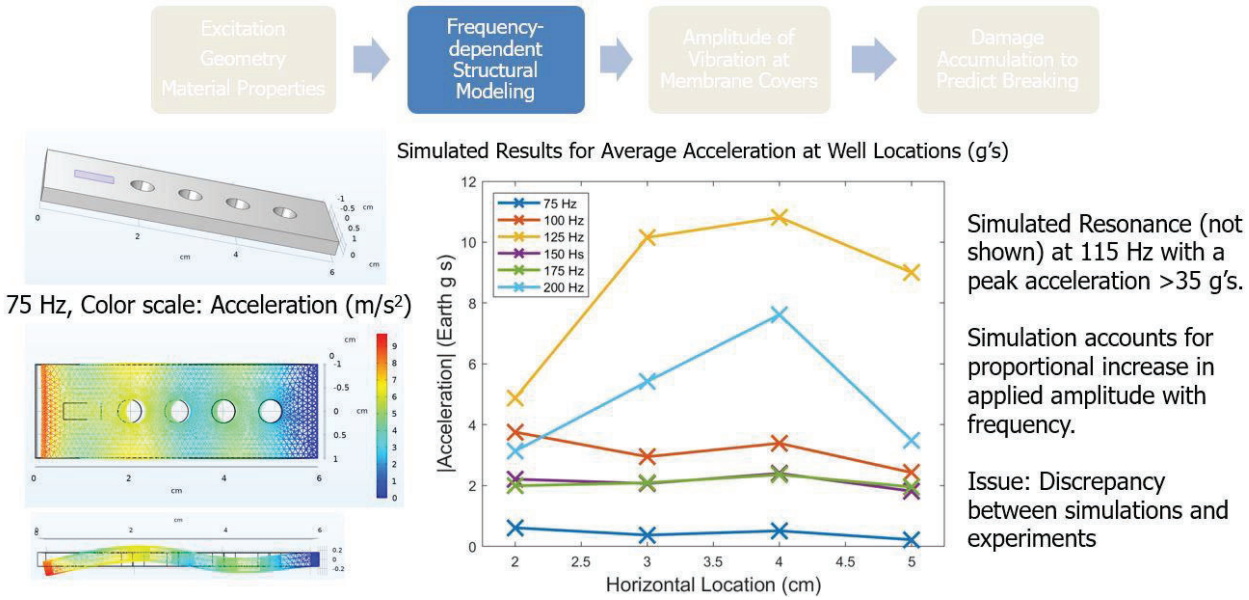

Figure 32: Defining the local acceleration as a function of location along the PDMS slab structure.

The third phase of the simulation shown in **Figure 33** involved building on original comparisons between simulated modes of vibrating membranes and analytical responses with specified diameters, thicknesses, added mass, and material properties. We visualized the axisymmetric rings of stress given an amplitude and frequency of vibration. In fact, we even built an "app" for COMSOL to allow us to quickly run through multiple scenarios and responses with applied loads to permit comparisons with experiments.

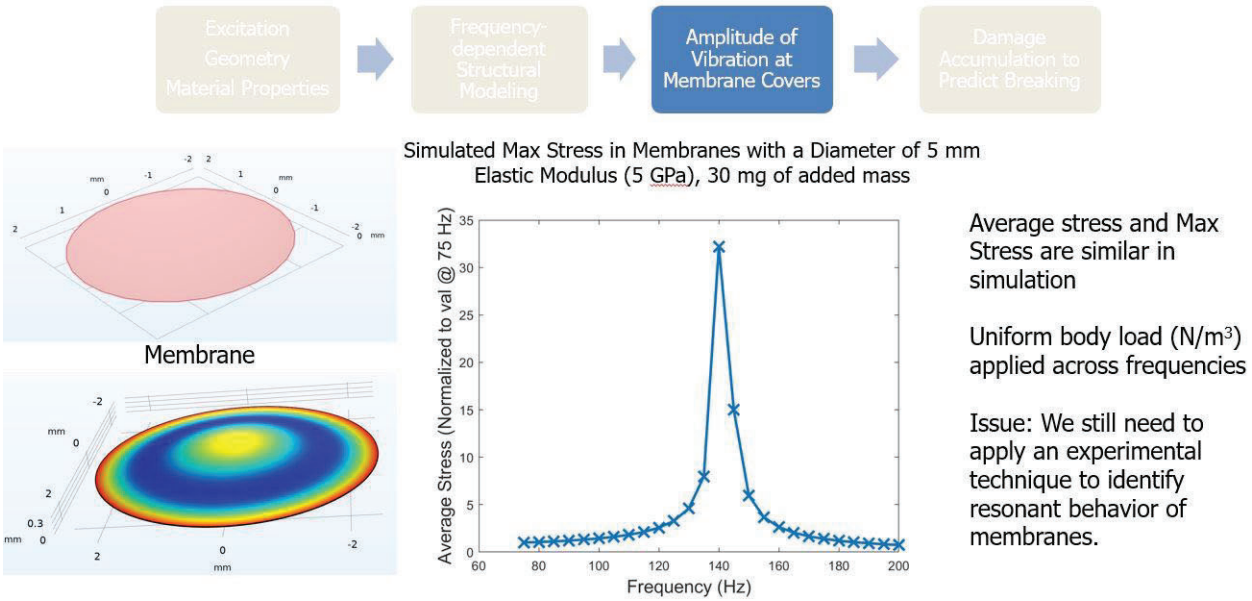

Figure 33: Defining characteristics of the membranes included their thickness, diameter, added mass, and material properties. An applied oscillatory load resulted in varied average stresses dependent on frequency.

Combining the two models – one for the structure and one for the membrane – with the multiplication of their frequency responses (similar to convolving two linear-time-invariant systems) allows us to predict the response of the membrane without a high-fidelity model. As shown in **Figure 35**, we can multiple the acceleration measured at a location on the structure against the normalized stress predicted at a specified frequency. We can also begin to think about ways to relate the vibration amplitude to accumulated damage in a fatigue-based model with an S (load/stress) – N (number of cycles) curve shown in **Figure 35**. This effort still needs more work to match with experimental data.

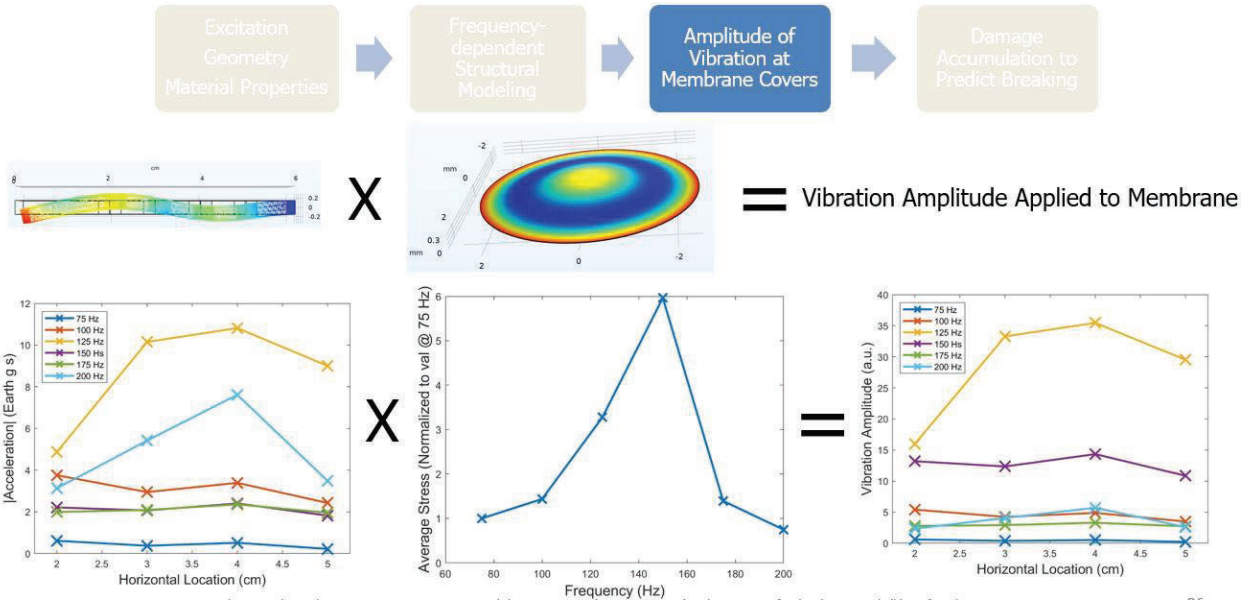

Figure 34: Combining the frequency responses for these two FEA models through multiplication (something similar to convolution in the time domain) permits the analysis of a metric for the vibration amplitude applied to the membrane

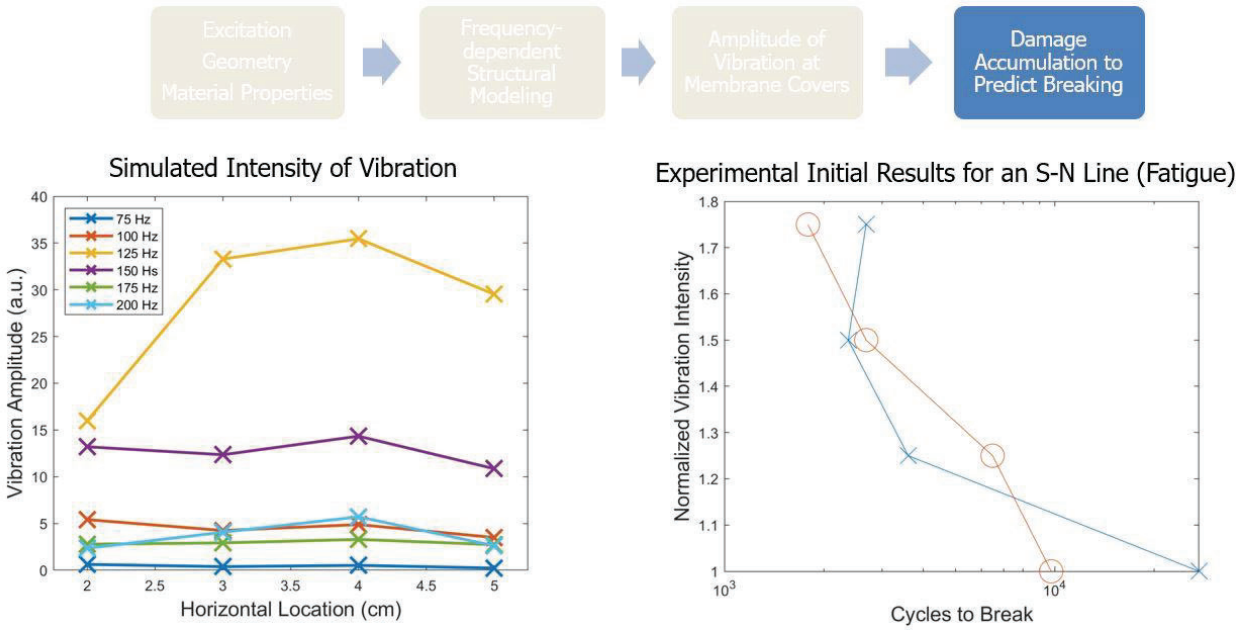

Figure 35: There is an opportunity to link the vibration amplitude to a set of fatigue-based S-N curves/relationships to predict the number of cycles required for low-cycle failure.

Error! Reference source not found.shows collected experimental data and how the amplitude and frequency of vibration are dependent on the voltage applied to the motor. We still do not have a complete link between the simulated results and the experimental results, but the simulations and these experiments helped guide us toward the final experimental results presented in the next section.

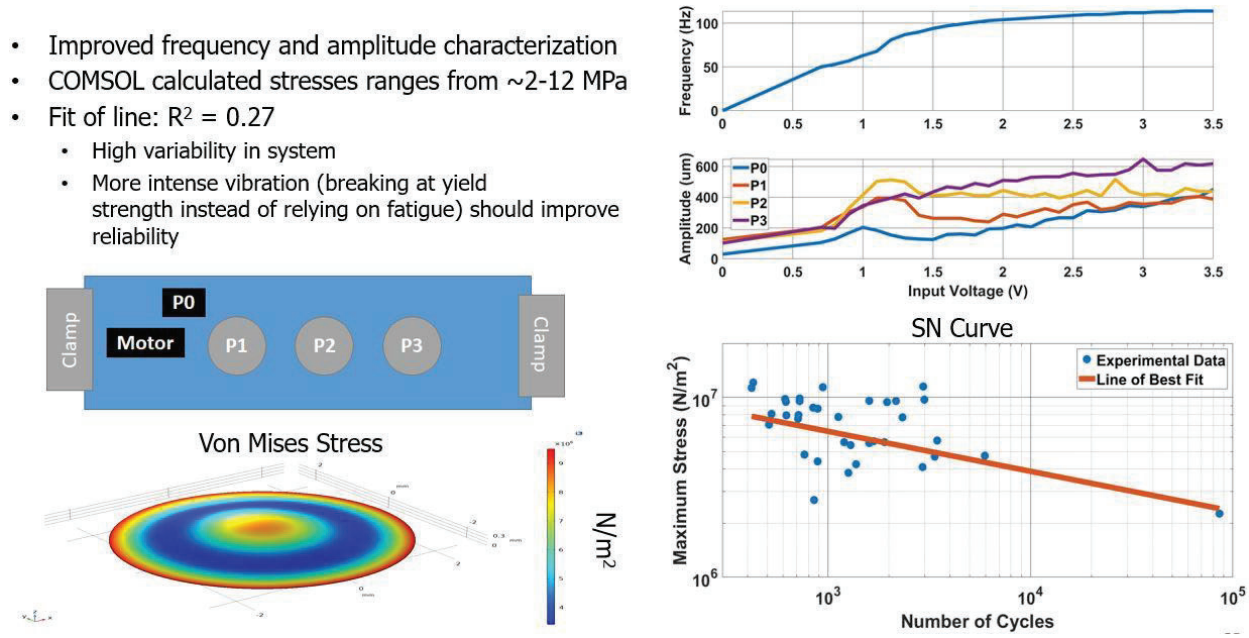

Figure 36: Collected experimental data to demonstrate how the number of cycles to failure is inversely proportional to the applied stress. There is still quite a bit of variability in these measurements.

3.8 Cover Selectivity with Membrane Size and Location

Based on the previous experimental and simulated data, we conceptualized a new 1x2 device with selected membrane locations and diameters. In this 2-cover system, the cover nearest to the motor is 4 mm in diameter with a small pinhole etched in the cover, and the farthest one is 5 mm in diameter. By applying a low voltage (2 V) followed by a higher voltage (4 V), covers break in the sequence nearest then farthest. When we reverse the voltage sequence, beginning with the high voltage (4 V) and then decreasing to the lower voltage (2 V), the breaking order is reversed (**Figure 37**). Thus, we were able to select the order of breaking between the two covers using a prescribed sequence of applied voltage to the motor. Changing the voltage changes the vibration amplitude "felt" by each of the covers, and applying the correct voltage can maximize amplitude at the location where breaking is desired.

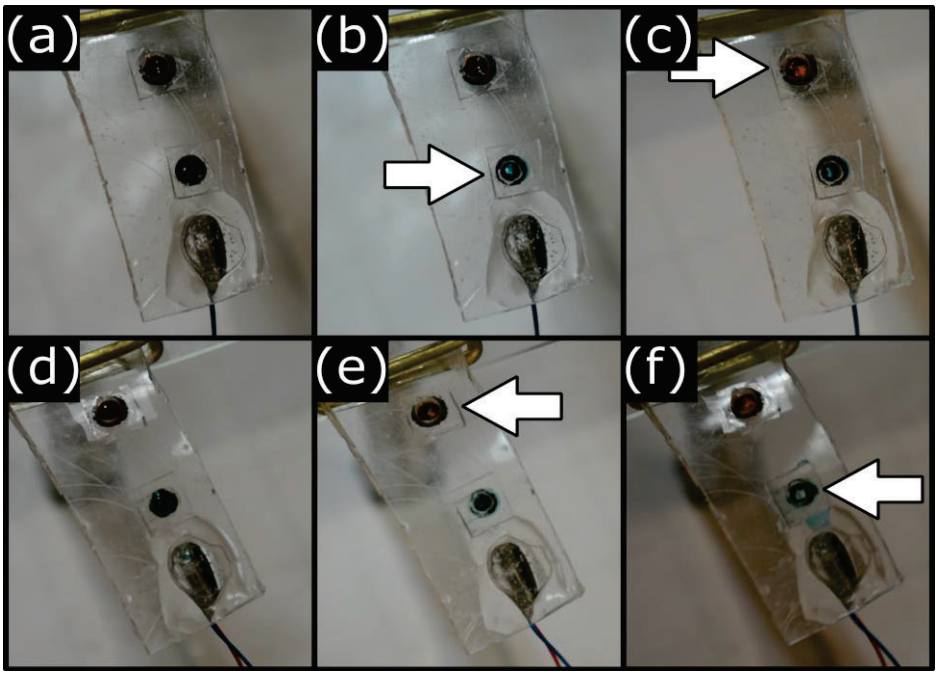

Figure 37: Changing breaking order on a 1x2 cover device. (a) Two unbroken covers on a single 1x2 device. Colored dye is in the well behind the cover, and is not visible as long as the cover is closed. (b) After running the motor at 2 V for 4 s, the cover nearest to the motor breaks, and blue dye is visible. (c) After running the motor for a further 2 s at 4 V, the farthest cover breaks and red dye is visible. (d) Another pair of unbroken covers. (e) After running the motor at 4V for 7 s, the farthest cover breaks. (f) After running the motor for a further 30 s at 2V, the nearest cover breaks.

With control achieved in a 2x1 cover device, we designed a 2x2 array cover device. Two motors were embedded at opposite end of the PDMS slab, thus creating what appeared to be two 2x1 devices next to each other on the same slab. However, as we began tests with a single motor, we found that one motor was able to break the four membranes in a specific order by increasing voltage from 2.6 to 3.5 V (**Figure 38**).

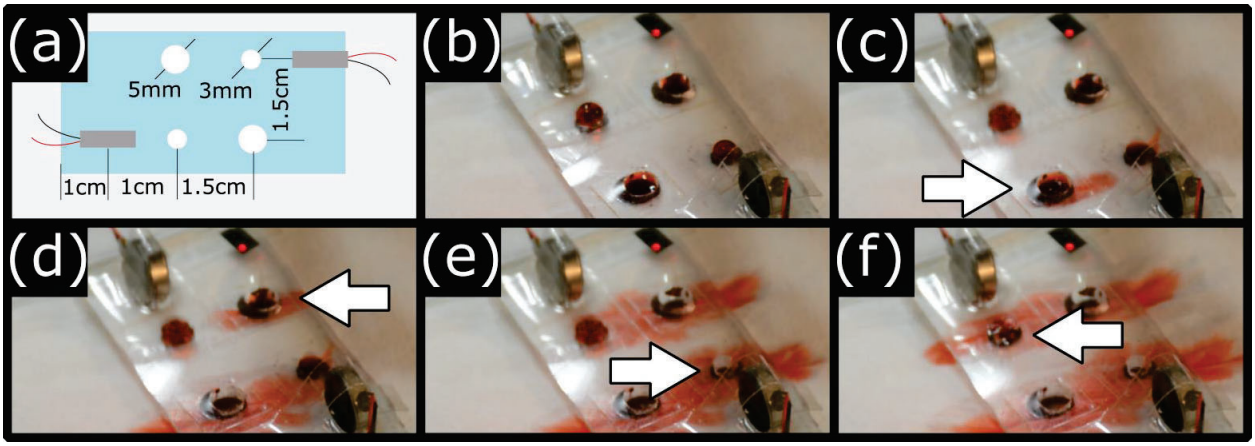

Figure 38: Vibration-induced membrane breaking on a 2x2 cover array. (a) Diagram of the 2x2 cover layout. The wells are 3 mm diameter in positions nearest the motors, and 5 mm diameter in the positions furthest from the motors. (b) Initial test layout, with each well containing 30 uL of red dyed water. (c) The top left motor is run for an average of 10 s at 2.6V to break the cover shown. (d) The motor is run for a

further 19 s to break the second cover shown. (e) Input voltage increased to 3V, and the third cover shown breaks after another 14 s. (f) The final cover is broken by running at 3 V for another 33 s.

With ordered breaking repeatable across several tests, we assembled the covers with sensor wells below covers (**Figure 39A,B**). Due to the support glass footprint on the sensors, only two wells could be tested simultaneously. P2 and P4 were selected to test and sensor data are shown in **Figure 39 C**. PBS (30 uL) was pipetted onto the covers 30 s before the motor was run. The two covers are shown breaking with a ~10 s delay for P2, and then another ~10 s between P2 then P4. The motor was turned off at 70 s. The output voltage is zero before well opening due to the sensor being dry (thus impedance is very high), and voltage increases to reach a plateau within 10-15 s of membrane opening. The short delay in reaching a stable voltage reading is not expected to significantly impact the impedance readout to samples containing analyte, since the timescale for the impedance to stabilize due to analyte-antibody binding in the sensor was on the order of hundreds of seconds (as previously shown in **Figure 6**).

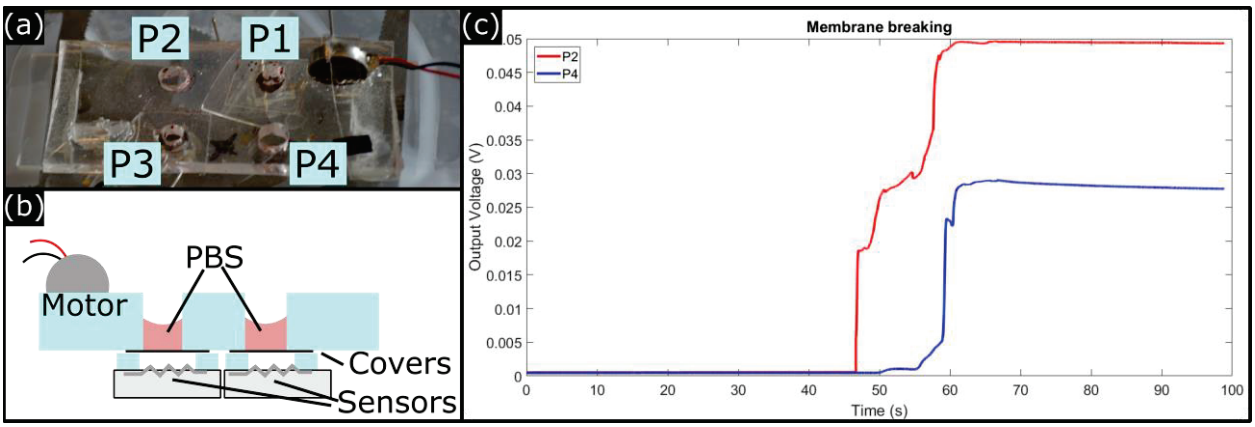

Figure 39: Sensor measurements during selective cover opening. (a) 2x2 device setup with wells labelled P1-P4. Only P1 and P3 have sensors attached in the photo. (b) Diagram of well setup, with PBS loaded on covers. Sensors are in air before breaking. (c) Sensor voltage during loading and breaking of covers. Covers P2 and P4 are loaded with PBS at 10 s, and motor is given 2.6V at 35 s. P2 breaks at 46 s, followed by P4 breaking at 55 s.

4 ONGOING WORK, CHALLENGES, AND FUTURE OPPORTUNITIES

The initial project aims can be summarized as follows: (1) to develop an array of 2 x 2 sensor patches that could measure up to 3 soluble biochemical factors in wound fluid, either ex vivo or in situ on the wounds themselves, and in a format that could fit in a “smart bandage”; (2) to develop a mechanism for on-demand sensing enabling one sensing device to gather data over time (up to 4 times in a 24 hour period) and in different spatial locations over a 1 cm x 1 cm wound without having to remove the device.

For the first aim, the sensing technology was shown to work extremely well in wound fluid samples and even when sensors were applied directly onto the wound bed in experimentally induced wounds in mice. We have designed sensors that measure TNF-α, IL-6, and albumin. The fourth sensor in 2 x 2 sensor patches would be used to track baseline, using a nonspecific antibody. Furthermore, we have been able to design a CMOS chip that can accurately measure the impedance change due to antigen binding over a wide concentration range. Although individual sensors were developed, we have not yet assembled the 2 x 2 array, which requires adding more input channels and switching capability to the flexible PCB that support the CMOS impedance analyzer. So far our PCB can handle signals from 2 nanowell sensing patches, which will have to be increased to 4. We will seek further miniaturization of the system as well, in order to enable the 2 x 2 sensor array to fit within a ~1 cm^2 area. The individual sensor patches in the array measure only 20 μm x 20 μm; thus, to accomplish this goal there is no need to change the fundamental design of the sensor itself. The main challenge will be to etch multiple sensors on one glass substrate, and improve packaging of the circuitry so that it fits in a smaller area.

For the second aim, we developed a graphene oxide membrane cover for the sensors that opens when it is induced to vibrate using a vibration motor (although other vibration sources, such as sound waves might be used as well). On the one hand, this approach was potentially advantageous because the mechanical stimulus can be transmitted to the membrane from relatively long distances and thus the vibration source does not need to be incorporated into the sensing platform. Furthermore, this method obviates the need to deliver relatively large currents in the vicinity of the sensors, as would be needed if electrothermal- or electrolysis-sensitive covers were to be used. On the other hand, we found that transmission of mechanical vibration throughout the structure is a relatively complex phenomenon, and as a result, vibration amplitude varied in nonobvious ways as a function of location. Thus, we were not able to complete the design and operation demonstration of the on-demand sensor within the grant performance period. Preliminary understanding of the mechanical phenomena using COMSOL modeling was however possible, and further studies will be carried out to systematically design the mechanics and geometry of the system so that sensor wells can be located and opened at desirable locations. Furthermore, we found that the number of vibrations to cause membrane opening was highly variable, which we attribute to the fact that a fatigue mechanism seems to be at play in the membrane cover rupturing process. We hypothesize that more reliable opening of the membrane may be possible if a small defect is incorporated into the membrane cover itself, such as a small notch or pinhole, which may promote a rapid fracture propagation mechanism when mechanical stress is applied. Once the basic opening mechanism is made to be reliable, we will explore ways to selectively open sensor wells over 2 x 2 sensor arrays.

Once the technology developments discussed above have sufficiently advanced, we will return to animal studies and explore the function of the biochemical sensing bandage on mouse wounds. It will be interesting to compare different wound sizes and wounds in animals with underlying diseases that slow down skin healing (such as diabetes and

spinal cord injury) to ultimately see if biochemical sensing data measurements over time provide an early prediction of the time to wound closure.

5 CONCLUSIONS

Nanowell sensors measuring about 2 μm in diameter and less than 100 nm high, containing one electrode at the bottom and one near the top, were developed. The nanowells were organized into 5x5 patches measuring a total of about 20 μm wide. Nanowells were pre-adsorbed with specific antibodies and the impedance measured between the two electrodes in the nanowells was sensitive to the amount of antigen that bound to the antibodies on the nanowell surfaces in a concentration-dependent manner. Antibody-based nanowell sensors were made to measure mouse wound levels of IL-6, TNF–α, and albumin. These sensors are extremely versatile since a new marker can be measured by changing the antibody used to pre-coat the sensor wells. The sensors were tested on mouse wound fluid samples ex vivo, as well as directly on the mouse wounds. The sensors were able to measure marker levels in the range of 10 to 1000 pg/mL, and the data were validated using standard biochemical assays.

The sensors were used to monitor the healing progression of standard dorsal skin wounds in mice. IL-6 and TNF–α peaked early, most likely reflecting the inflammatory phase of healing, while albumin peaked later during the proliferative phase of healing just before the wounds closed. An extensive search for additional markers that would exhibit different dynamics showed that many factors that are expected to rise later in the wound healing cascade did not in fact do so but rather peaked during the inflammation phase. Because the sensors measure cytokine and chemokine levels in fluid expressed from the wound, those levels reflect not only what wound cells produce, but also how much is transported out into the wound fluid, which also depends on wound fluid production at that stage. Thus, gene expression levels that indicate when certain factors should be elevated do not necessarily correlate with the appearance of these factors in wound fluid.

Several nanowell patches can be connected to the same impedance analyzer with the appropriate multiplexing hardware. A custom-made CMOS was developed that could effectively replace the large benchtop impedance analyzer, which was incorporated into a flexible printed circuit board allowing switching between two different nanowell patches. The same principle could be easily extended to drive multiple nanowell patches. The circuitry (including a battery) could be housed in a bandage form factor thus allowing wound monitoring over time.

A limitation of the antibody-based sensors is their lack of dynamic sensing because the antigens do not easily come off the sensors. Operating sensors in complex biological fluids is also fraught with potential problems due to fouling and also sensor drift over time. Our approach was to make sensors essentially disposable, to be used only once,

thus avoiding those complexities altogether. In order to control the timing of sensing, without having to physically remove and replace sensor patches from the wound, sensor covers made of graphene oxide membranes were devised. The sensor patches are placed inside small silicone rubber wells which are then covered with the membranes. Membrane opening was triggered using a vibration-driven mechanism. Membrane diameter and thickness determine a mechanical resonant vibration frequency, which can be induced if a vibration generator, tuned at the correct frequency, is placed in the vicinity. Using membranes of different diameter and different frequencies, it was possible to open wells in a prescribed fashion. The vibration-mediated process makes it possible to implement in a variety of geometries and without complex wiring. However, additional and unexpected complexities were found with this approach. In particular, the use of a flexible support for the sensor wells and their covers causes the formation of nodes where vibration is strongly attenuated. In other words, vibration amplitude was not unform throughout the structure, and further studies are needed to optimize the support geometry and its mechanical properties, as well as the precise location of the cover membranes to make this approach more reliable and able to handle multiple sensor patches.

6 REFERENCES

1. Mostafalu P, Tamayol A, Rahimi R, Ochoa M, Khalilpour A, Kiaee G, Yazdi IK, Bagherifard S, Dokmeci MR, Ziaie B, Sonkusale SR, Khademhosseini A. Smart Bandage for Monitoring and Treatment of Chronic Wounds. Small. 2018:e1703509. doi: 10.1002/smll.201703509. PubMed PMID: 29978547.
2. Eming SA, Wynn TA, Martin P. Inflammation and metabolism in tissue repair and regeneration. Science. 2017;356(6342):1026-30. doi: 10.1126/science.aam7928. PubMed PMID: 28596335.
3. Scaffidi P, Misteli T, Bianchi ME. Release of chromatin protein HMGB1 by necrotic cells triggers inflammation. Nature. 2002;418(6894):191-5. doi: 10.1038/nature00858. PubMed PMID: 12110890.
4. Hettiaratchy S, Dziewulski P. ABC of burns: pathophysiology and types of burns. BMJ. 2004;328(7453):1427-9. doi: 10.1136/bmj.328.7453.1427. PubMed PMID: 15191982; PMCID: PMC421790.
5. Chanmugam A, Langemo D, Thomason K, Haan J, Altenburger EA, Tippett A, Henderson L, Zortman TA. Relative Temperature Maximum in Wound Infection and Inflammation as Compared with a Control Subject Using Long-Wave Infrared Thermography. Adv Skin Wound Care. 2017;30(9):406-14. doi: 10.1097/01.ASW.0000522161.13573.62. PubMed PMID: 28817451.
6. Zomer HD, Trentin AG. Skin wound healing in humans and mice: Challenges in translational research. J Dermatol Sci. 2018;90(1):3-12. doi: 10.1016/j.jdermsci.2017.12.009. PubMed PMID: 29289417.
7. Zhu C, Wen Y, Liu T, Yang H, Sengupta K, editors. A Packaged Ingestible Bio-Pill with 15-Pixel Multiplexed Fluorescence Nucleic-Acid Sensor and Bi-Directional Wireless Interface for In-Vivo Bio-Molecular Sensing. 2020 IEEE Symposium on VLSI Circuits; 2020 16-19 June 2020.
8. Xie P, Tayyab M, Ashraf A, Kumar S, Mazzeo A, Sengupta K, Berthiaume F, Javanmard M, editors. Real Time Cytokine Quantification in Wound Fluid Samples Using Nanowell Impedance Sensing. 2021 21st International Conference on Solid-State Sensors, Actuators and Microsystems (Transducers); 2021 20-24 June 2021.
9. Zhu C, Maldonado J, Tang H, Venkatesh S, Sengupta K, editors. 18.2 CMOS-Driven Pneumatic-Free Scalable Microfluidics and Fluid Processing with Label-Free Cellular and Bio-Molecular Sensing Capability for an End-to-End Point-of-Care System. 2021 IEEE International Solid- State Circuits Conference (ISSCC); 2021 13-22 Feb. 2021.
10. Liu S, Hu K, Cerruti M, Barthelat F. Ultra-stiff graphene oxide paper prepared by directed-flow vacuum filtration. Carbon. 2020;158:426-34. doi: https://doi.org/10.1016/j.carbon.2019.11.007.
11. Krueger M, Berg S, Stone D, Strelcov E, Dikin DA, Kim J, Cote LJ, Huang J, Kolmakov A. Drop-casted self-assembling graphene oxide membranes for scanning electron microscopy on wet and dense gaseous samples. ACS Nano. 2011;5(12):10047-54. doi: 10.1021/nn204287g. PubMed PMID: 22103932.
12. Shao J-J, Lv W, Yang Q-H. Self-Assembly of Graphene Oxide at Interfaces. Advanced Materials. 2014;26(32):5586-612. doi: https://doi.org/10.1002/adma.201400267.

LIST OF SYMBOLS, ABBREVIATIONS, AND ACRONYMS

%	percent
ºC	celsius
cm	centimeter
CMOS	complementary metal-oxide-semiconductor
CN	cellulose nitrate
DAMPs	damage-associated molecular patterns
ELISA	enzyme-linked immunosorbent assay
ETD	Everhart-Thornley detector
FEA	finite element analysis
g	gram
GO	graphene oxide
HMGB1	high-mobility group box 1
Hz	hertz
IACUC	Institutional Animal Care and Use Committee
IL-6	interleukin-6
kΩ	kiloohms
kHz	kilohertz
LO	local oscillator
mm	millimeter
um	micrometer
mL	milliliter
mN	millinewton
MUX	multiplexer
ng	nanogram
nM	nanomolar
NW	nanowell
PBS:	phosphate-buffered saline
PCB	printed circuit board
PDMS	polydimethylsiloxane
pg	picogram
pM	picomolar
S	seconds
SDF-1	stromal-derived factor-1
SEM	scanning electron microscopy
SPI	Serial Peripheral Interface
TNF-α	tumor necrosis factor-alpha
uA	microamperes
uL	microliter
V	voltage
VEGF	vascular endothelial cell factor

APPENDIX – LIST OF PRESENTATIONS AND PUBLICATIONS

Transducers 2021:
Pengfei Xie; Muhammad Tayyab; Ali Ashraf; Suneel Kumar; Aaron Mazzeo; Kaushik Sengupta; François Berthiaume; Mehdi Javanmard, "Real Time Cytokine Quantification in Wound Fluid Samples Using Nanowell Impedance Sensing," 2021 21st International Conference on Solid-State Sensors, Actuators and Microsystems (Transducers), 2021, pp. 779-782, doi: 10.1109/Transducers50396.2021.9495529.

Hilton Head 2022:
Chengjie Zhu; Pengfei Xie; Ryan Thorpe; Jesus Maldonado; Suneel Kumar; Aaron Mazzeo; Mehdi Javanmard; Francois Berthiaume; Kaushik Sengupta, “CMOS-nanowell-based Hybrid Smart Bandage for Long Term Monitoring of Wound Healing Via Cytokine Quantification In-situ,” 2022 Hilton Head Solid-State Sensors, Actuators and Microsystems Workshop.

Biomedical Engineering Society 2022 (planned):
Suneel Kumar; Pengfei Xie; Chengjie Zhu; Aaron Mazzeo; Kaushik Sengupta; Mehdi Javanmard; Francois Berthiaume, “Wound Fluid Marker Dynamics Correlate with Wound Healing Stage in Mouse Model”

ASME-iMECE 2022 (planned):
Stephen Mclaughlin; Ali Ashraf; Pengfei Xie; Suneel Kumar; Kaushik Sengupta; Mehdi Javanmard; Francois Berthiaume; Aaron Mazzeo, “Vibration-Actuated Sensors for Wound Fluid Biomarkers”